Morphing wing design using integrated and distributed trailing edge morphing

Mkhoyan, Tigran; Thakrar, Nisarg R.; De Breuker, Roeland; Sodja, Jurij

DOI
10.1088/1361-665X/aca18b

Publication date
2022

Document Version
Final published version

Published in
Smart Materials and Structures

Morphing wing design using integrated and distributed trailing edge morphing

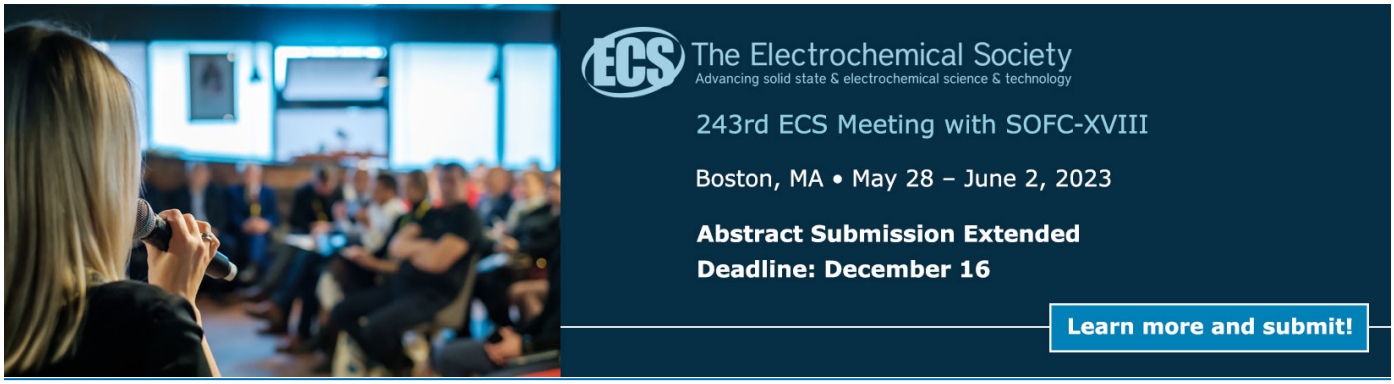

OPEN ACCESS
IOP Publishing
Smart Materials and Structures
Smart Mater. Struct. **31** (2022) 125025 (20pp)
https://doi.org/10.1088/1361-665X/aca18b

Morphing wing design using integrated and distributed trailing edge morphing

Tigran Mkhoyan*, Nisarg R Thakrar, Roeland De Breuker and Jurij Sodja

Faculty of Aerospace Engineering, Aerospace Structures and Materials Department, Delft University of Technology, PO Box 5058, 2600GB Delft, The Netherlands

E-mail: T.Mkhoyan@tudelft.nl

Received 21 February 2022, revised 24 October 2022
Accepted for publication 9 November 2022
Published 25 November 2022

Abstract

The presented study investigates the design and development of an autonomous morphing wing concept developed in the scope of the SmartX project, which aims to demonstrate in-flight performance optimisation with active morphing. To progress this goal, a novel distributed morphing concept with six translation induced camber morphing trailing edge modules is proposed in this study. The modules are interconnected using elastomeric skin segments to allow seamless variation of local lift distribution along the wingspan. A fluid-structure interaction optimisation tool is developed to produce an optimised laminate design considering the ply orientation, laminate thickness, laminate properties and actuation loads of the module. Analysis of the kinematic model of the integrated actuator system is performed, and a design is achieved, which meets the required continuous load and fulfils both static and dynamic requirements in terms of bandwidth and peak actuator torque with conventional actuators. The morphing design is validated using digital image correlation measurements of the morphing modules. Characterisation of mechanical losses in the actuator mechanism is performed. Out-of-plane deformations in the bottom skin and added stiffness of the elastomer are identified as the impacting factors of the reduced tip deflection.

Keywords: active morphing, design optimisation, bio-inspired, distributed, over-actuated, over-sensed

(Some figures may appear in colour only in the online journal)

Nomenclature

Acronyms

AOA	Angle of Attack, °
DIC	Digital Image Correlation
FBD	Free-Body Diagram
FEM	Finite Element Model
FSI	Fluid-Structure Interaction
LE	Leading Edge
TE	Trailing Edge
TRIC	Trailing Edge Induced Camber

Symbols

δ_a	actuator rotation, °
δ_l	angle between F_a and F_l, °
C_L	coefficient of Lift
F_a	actuator force, N
F_l	linkage force, N
F_r	reaction force at linkage, N
M_x, M_y, M_z	nodal moment around x,y,z axes, Nm
r_a	torque arm length, m
rho	air density, kg m^3
T_a	actuator torque, [Nm]
V_∞	air speed, m s^{-1}

* Author to whom any correspondence should be addressed.

x,y,z	nodal displacement along x,y,z axes, m
x_a	actuator horizontal deflection range, Nm
c_p	aerodynamic pressure coefficient

Subscripts

1,2	actuators left and right of module
lin,non-lin	linear, non-linear coefficient

Superscripts

aero	coefficient calculated on the aerodynamic mesh
fem	coefficient interpolated on the FEM mesh
max,min	maximum and minimum values

1. Introduction

The advancements in aerospace materials, manufacturing technology, controller and hardware design allow developing increasingly lighter and more complex concepts such as morphing wings, which significantly benefit flight performance. Initially inspired by avian biology, the effectiveness of such concepts is demonstrated in nature, with wing shape adaptation and optimal gliding performance [1, 2]. As in nature, morphing wing concepts have evolved since the early years of aviation. One of the well-documented examples was the active roll control of the Wright Flyer, the first successful heavier-than-air powered aircraft. In this lightweight design, the lateral stability was ensured by wing twist-warping [3]. In this case, the flexible fabric-wrapped structure was well suited for morphing. However, as the flight speeds and loads were increased with the advancement of aircraft design, a stiffer wing was required to fulfil load requirements and overcome aeroelastic instabilities. As a result, the conventional rigid wing design, generally optimised for cruise, exhibits compromised performance in other flight conditions. More importantly, due to continuous fuel burn and redistribution of the weight, no optimal configuration can be found which is met through the entire cruise phase. Active morphing has the potential to reduce this performance gap and continuously optimise the aircraft performance across the entire flight envelope adaptively. However, a challenging aspect in active morphing is designing a feasible and effective morphing mechanism such that the aircraft performance can be improved actively throughout the flight envelope [4]. That is the subject of this paper.

In literature, various morphing concepts can be found. A comprehensive review of the early morphing concepts of various approaches regarding the actuator material, the actuation mechanism, and the skin types is found in [5]. Examples vary from conventional to compliant mechanisms and materials in the latter two categories. Also, various materials are investigated for the actuators, ranging from conventional to piezoelectric and shape memory alloys. In aircraft wings, morphing can be applied to the LE, TE, or both.

Kintscher *et al* and Sodja *et al* investigate a seamless morphing droop nose concept for the LE, designed to match a given target shape with different materials used for the morphing skin such as glass-fibre pre-preg and aluminium [6, 7]. The concept by Sodja *et al* utilises conventional actuation. Here, low actuation forces are achieved by maintaining the skin length constant during morphing, such that strains in the skin are kept minimal. Several other concepts achieve low actuation force by utilising compliant skin, and actuation mechanisms [8–10]. While promising, the studies highlight the importance of further research into manufacturing and up-scaling complex compliant designs since the manufacturing process of these complex shapes is still challenging.

Further, examples of the compliant mechanism and actuation are investigated. Previtali *et al* used conventional actuators, and Molinari *et al* used piezoelectric skin actuation [9–12]. Some studies use bio-inspired design, such as the Fish-BAC concept, designed to mimic the compliant skeletal frame of fish, developed at Swansea University [13–15]. TE mechanisms are also presented by FlexSys, which have been installed and undergone flight tests on a modified Gulfstream III business jet [9, 16, 17].

Recent studies also investigated the use of ultralight, lattice-based structural modules assembled in a modular adaptive structure using carbon fibre-reinforced polymers (CFRPs) [18–20]. The advantage is that these materials can have the stiffness of a typical elastomer at the mass-density typical to aero-gel. Cremer *et al* [19] demonstrate improved aerodynamic efficiency and roll control authority with spatially programmed elastic morphing shape of a 4.27 m wingspan aircraft in the wind tunnel. Jennet *et al* [18] present the digital morphing wing concept, constructed from discrete lattice elements. This concept shows increased roll efficiency compared to a conventional wing by applying span-wise twisting deformation. While promising, due to its programmable flexibility and lightweight, the lattice-based modules occupy most of the internal space. Therefore, additional consideration is needed to ensure the flexibility of the structure while reserving the room for fuel, batteries, and other components to be installed in the wing. The lattice-based concept, presented by Keidel *et al* [20], suggests a potential structurally efficient approach through optimisation of the orientation and distribution of the CFRP rods. However, additional consideration is needed for larger wing structures and manufacturability aspects for this concept.

In addition to the internal actuation mechanisms, the concept of morphing through direct skin actuation was investigated by Bilgen *et al* with piezoelectric actuators [21, 22]. Pankonien *et al* investigated skin actuation with macro fibre composite actuators for camber morphing [23]. Another wing concept by Mistry and Gandhi demonstrated a cross-sectional warping mechanism to realise variable camber on a rotor blade [24].

Another study developed under NASA Advanced Air Transport Technology investigated the multi-flap variable camber continuous trailing edge flap (VCCTEF) concept for generic transport model (GTM) [25]. This concept demonstrated effectiveness in multi-objective control and gust load alleviation in [26, 27]. However, the real-life experimental demonstrator with shape memory alloys (SMA) rotary actuators revealed many challenges such as weight effectiveness, speed and power requirements of the actuators, the complexity

of multi-segment camber mechanism, and skin flexibility required [25].

In a recent study conducted in the EU FP7 CHANGE project, a morphing concept called the translation induced camber (TRIC) is introduced to address some of these problems [28]. This concept implements a relatively simple and effective morphing mechanism that uses a combination of cross-sectional warping and skin bending to induce both camber and twist morphing with a pair of conventional actuators. The advantage of this concept is its relative simplicity and compactness of the actuation mechanism, which increases the fuel carrying capability and volume needed for necessary auxiliary components in the wing. However, the main disadvantage of the current TRIC concept is that the lift distribution cannot be influenced locally with a single morphing surface controlled by a single pair of actuators. As a result, this inhibits the use of the morphing mechanism for multi-objective flight control and limits its use as a direct replacement of conventional control surfaces for rigid body motion control (ailerons, rudders and elevators). Various control design studies highlight the necessity and effectiveness of multi-objective flight control, load alleviation, and drag reduction performed by distributed multi-flap systems such as the VCCTEF in [26, 27] and conventionally flapped over-actuated aircraft models [29].

Summarising, the literature survey suggests that many morphing concepts are restricted to either wing twist or camber morphing mechanisms, proposing a complex mechanism that introduces manufacturing challenges or consumes a large portion of the wing internal volume. Furthermore, most concepts show a global morphing approach, while in the scope of active control, a distributed and over-actuated mechanism is necessary to apply simultaneous gust and manoeuvre load alleviation, flutter suppression and drag minimisation.

The current study extends on the TRIC concept to address this problem. It introduces a distributed and modular morphing design interconnected with elastomeric skin segments to allow seamless active twist and camber morphing. This way, the lift distribution along the wingspan can be varied locally and actively without additional drag penalty due to the gaps between the control surfaces. Furthermore, it allows deploying multiple control surfaces for various control objectives. This morphing design was developed in the scope of an autonomous smart wing project called SmartX, which aims to demonstrate an integrated and coherent approach to multi-objective load alleviation, flutter suppression and performance optimisation of adaptive aircraft wings [30].

In figure 1 the rationale behind the integrated design of the SmartX wing is presented [31, 32]. The purpose of this technology demonstrator is to demonstrate performance optimisation of multiple objectives such as (a) drag optimisation, (b) load alleviation, (c) flutter suppression and (d) shape control through multidisciplinary utilisation of smart sensing, control, actuation, and integration [33].

weAddressing the shortcomings of the previous morphing designs, the contributions of this study are threefold. First, a distributed morphing concept is developed, analysed, and validated using DIC measurements. Second, solutions

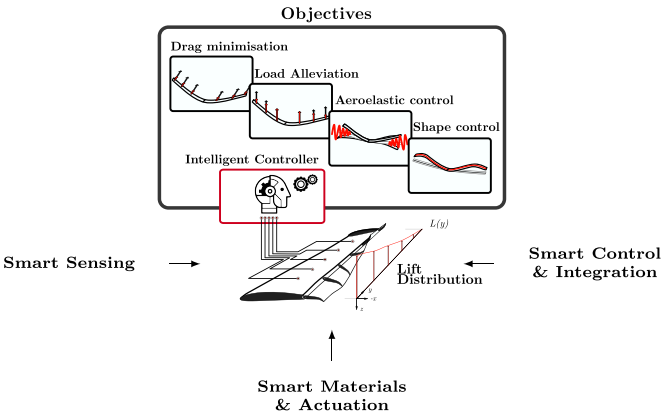

Figure 1. Rationale of the SmartX wing. Reproduced with permission from [31].

are investigated and implemented to improve the aerodynamic character and the continuity between adjacent morphing modules. Finally, a computationally efficient design framework is developed for analysis and design optimisation. This study aligns these objectives in the scope of the development of the SmartX-Alpha wing demonstrator.

This paper is structured in the following way. First, the scope of the SmartX project is presented in 1, followed by a brief overview of the TRIC and the design evolution of the distributed morphing concept in section 2. The design methodology, describing the development of the FSI tool and the design optimisation framework, are presented in section 3. The demonstrator manufacturing and integration are presented in section 4. The finalised design and the design validation are shown and discussed in section 5. Finally, conclusions are drawn in section 6.

2. Morphing concept

The TRIC concept served as the basis of the design [28]. The morphing concept underwent several stages of evolution, which led to the development of a fully composite smart morphing wing concept, named the SmartX-Alpha demonstrator. The motivation for the development of this demonstrator is explained in section 1, the design evolution of distributed TRIC concept is discussed in sections 2.1 and 2.2.

2.1. TRIC overview

The literature review highlighted some shortcomings of the previous morphing designs, which are addressed to a degree by the TRIC concept developed in CHANGE [28]. The crux of the TRIC is to utilise a combination of cross-sectional warping and skin bending to induce camber and twist morphing powered by conventional actuators. Due to its relative simplicity and compactness, the mechanism is economical in weight and size. The following section explains how the TRIC concept has evolved from design stages I–III as illustrated in figure 2. In this figure, sections of the morphing wing are

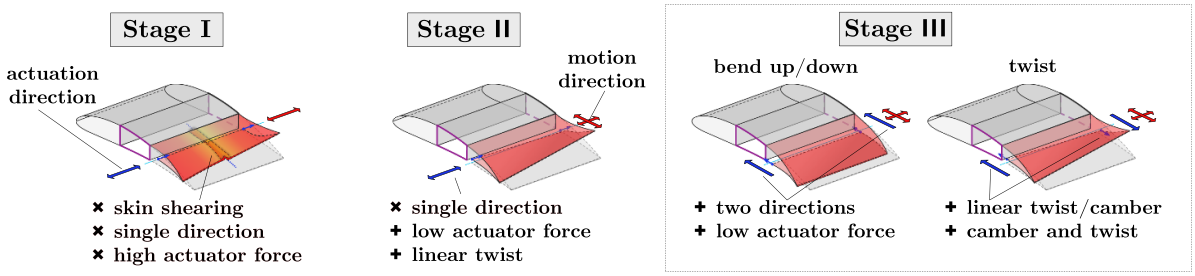

Figure 2. TRIC morphing concept design evolution stages I–III by Werter *et al* [28].

depicted, with the red area indicating the morphing skin and purple outline, the wing box. The direction of actuation is indicated with blue arrows and the direction of motion of the skin in red.

TRIC concept is derived from the principle of a warping cross-section [34], first introduced by Vos *et al* with a twist morphing concept. The first design stage of TRIC, similar to the latter concept, introduces a cut along the span on the bottom of the wing and utilises span-wise actuation, without any chord-wise movement (Stage I of figure 2). The span-wise actuation provides the intended warping of the skin; however, since the wingbox is relatively stiff in comparison, shearing of the skin is also introduced. This results in relatively large actuation forces and non-linearity in span-wise twist distribution. In the next stage of design evolution, Stage II in the middle of figure 2, chord-wise motion is allowed, as indicated by the red arrow. As a result, shear deformations are significantly reduced, leading to lower actuation forces and smooth linear twist distribution along the span. However, only twist morphing is possible since the chord-wise motion is coupled to span-wise actuation. In the final stage, stage III, the actuation direction is changed from span-wise to chord-wise, and both camber and twist morphing can be commanded independently while the actuation forces are low. By altering the actuation direction, two sets of actuators moving either symmetrically (in the same direction) or asymmetrically (in the opposite direction) can now introduce pure camber morphing (Bend Up/Down) or warp-induced span-wise twist morphing (Twist), as shown in the last column of figure 2.

2.2. Distributed morphing

In stage III, the TRIC concept achieves an efficient compact design, where the actuation forces are kept low, and the internal space is not compromised. While promising, a single-pair TRIC actuator design has a significant limitation: a single control surface spans the entire wing. Hence, neither camber nor twist can be controlled locally.

Therefore, from the perspective of control design, the actuator system cannot satisfy multiple objectives simultaneously. Generally, the typical approach is to separate the control tasks over the available control surfaces when control design must address multiple objectives [35, 36]. To prevent conflicts between various tasks such as pitch control, roll control or load alleviation, the control surfaces are either assigned to specific tasks [37]. Another possibility for conventionally

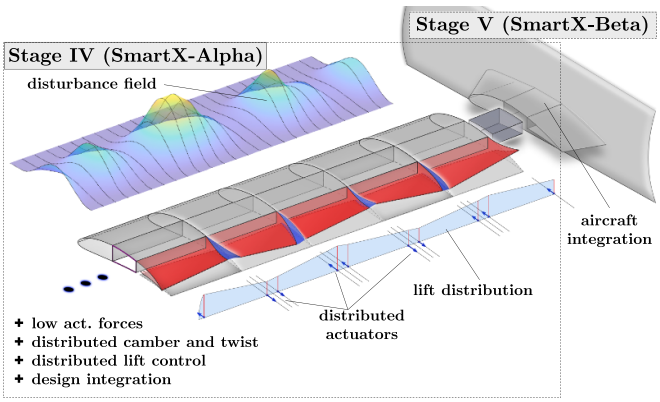

Figure 3. Distributed TRIC morphing concept, the SmartX-Alpha, investigated in this study.

actuated flexible aircraft is to make a compromise between the objectives, as reported in [38]. The conflict can be prevented if the aircraft features a sufficiently high number of control surfaces such that several control tasks can be addressed simultaneously. This would allow addressing both the attitude control of the aircraft body (pitch, roll, yaw) and aeroelastic control (load alleviation, flutter control etc) by continuously adjusting the same set of control surfaces (control allocation) [29]. When combined with morphing, more objectives can be achieved in control architecture, such as shape and drag optimisation, leading to a more optimal lift distribution. Variable camber continuous trailing edge flap (VCCTEF) is an example of a multi-segment camber morphing concept integrated on a flexible wing GTM, where drag minimisation is demonstrated [26, 27]. However, the complexity of this multi-hinged distributed morphing design has restricted the development of the VCCTEF to mainly numerical studies.

Our study aims to contribute to the state-of-the-art morphing design and proposes a distributed modular morphing wing concept suitable for multi-objective control. The proposed concept extends on the simplicity of the TRIC concept and benefits from the smooth over-actuated morphing system. In this context, it investigates a solution for the discontinuity introduced by a distributed multi-flap system. In addition, the aim is to demonstrate the concept of a wind tunnel model called the SmartX-Alpha. This demonstrator includes six morphing modules, allowing the independent camber and span-wise twist morphing of local span segments. This design evolution is illustrated in stage IV in figure 3.

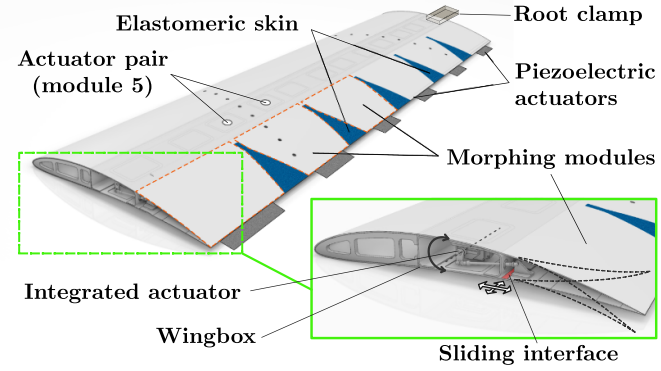

Figure 4. Overview of the SmartX-Alpha seamless TRIC morphing concept.

As with the TRIC concept, the skin is actuated internally, allowing smooth and seamless morphing along the chord. The morphing target shape is commanded using fast, high-torque servos embedded in the wing box. The servos allow the TE bottom skin to slide chord-wise and span-wise inside a guiding slot, as illustrated in the green zoomed-in box in figure 4. Each module has two actuators, allowing local symmetric (pure bending) and asymmetric (twist) morphing. Interconnected triangular skin segments, joined by an elastomer material, allow for continuous span-wise variation of the morphing wing shape, facilitating a continuous lift distribution over the wingspan. The triangular skin segments, illustrated in figure 4, are composed of elastomeric material.

The main advantage of the current design is that by adjusting the camber and twist distribution, the lift distribution can be controlled locally and independently for each module, allowing the wing to assume an optimal aerodynamic configuration to maximise lift-to-drag ratio to minimise drag. Furthermore, the lift distribution can be adapted to perform manoeuvre load alleviation when necessary by redistribution of the lift closer to the root of the wing. Lastly, fast piezoelectric actuators are placed at the tip of the morphing TE for aeroelastic control, such as flutter suppression, hereby covering the targets presented earlier in figure 1. To sustain the required loads, meet the actuator constraints, and achieve the desired morphing shapes, the composite skin of the wing is tailored and optimised. Therefore, a FSI structural optimisation tool is developed to allow fast analysis and optimisation of ply orientation and laminate thickness in terms of the given input loads, desired target shapes and actuator limits. The devised design methodology used in this assessment is presented in the next section.

3. Design methodology

The design methodology is centred around an FSI framework, with the aim of performing structural sizing of the morphing wing. The FSI framework connects the FEM and the aerodynamic model (XFOIL) to obtain a representative pressure load (PLOAD) for the structural sizing. The main goals of the FSI framework can be summarized as follows: (a) obtain PLOADs for structural optimisation of the morphing wing skin comprising the TE morphing control surfaces presented in section 2.2 and (b) allow initial assessment of the actuator loads and actuator input under static aerodynamic load for surrogate modelling and control design. Dynamic assessment of the morphing wing is not considered in the methodology.

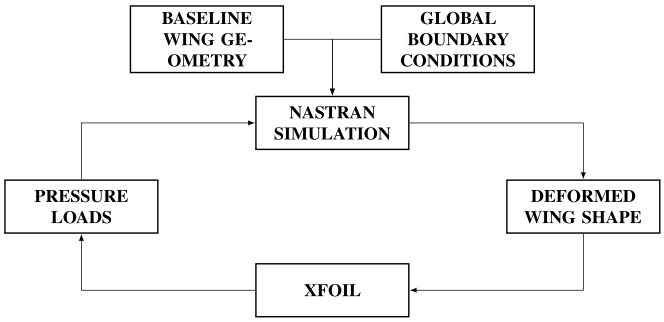

Figure 5. Flow chart of the FSI framework. Reproduced with permission from [31].

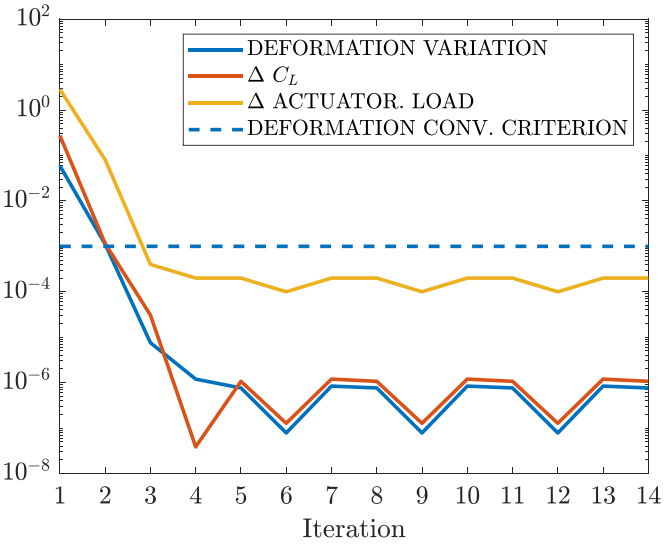

Figure 6. Convergence assessment of the FSI framework for actuator loads and δC_{L} for Bend down morphing condition. Reproduced with permission from [31].

3.1. FSI framework

The general flow diagram of the FSI framework is illustrated in figure 5 [31]. The NASTRAN FEM model [39] and the aerodynamic model represented by XFOIL [40] are coupled by the framework, in which MATLAB acts as the interfacing software.

The actuator displacement was used as input to the simulation for each loop iteration. Bend Up, Bend Down and Twist were considered as target morphing shapes. The loop was iterated until the deformed shape, lift, and actuation loads converged. Figure 6 shows the convergence of the FSI loop for the Bend Down case. As shown, the convergence of these variables is typically reached in three to four iterations [31]. Here, the progressive variation of these variables is shown over each

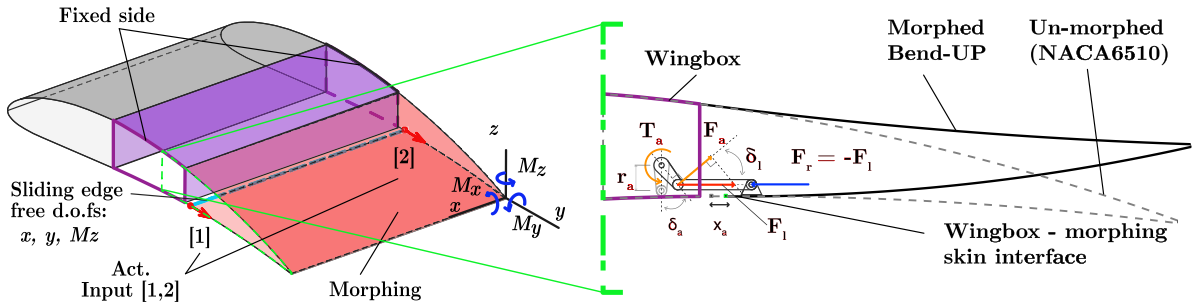

Figure 7. FEM model boundary conditions and actuator free body diagram.

iteration. The dotted blue line indicates the deformation convergence criterion of $1e-3$ evaluated as the cumulative variance of deformations over each node (continuous blue line). The convergence criteria and study are further discussed in section 5.1.

The actuator displacement was modelled by displacing the nodes, which acted as the interface between the actuator's pushrod and the skin. This is depicted in figure 7. The actuator displacement would, in turn, impose a deformation of the shape, which was extracted from NASTRAN and transferred to XFOIL to exact pressure distribution data. The pressure data was returned to the NASTRAN model as static PLOADs.

3.1.1. FEM. The FEM model, representing a morphing module of 500 mm chord and 300 mm span, was developed in NASTRAN [39]. A cut is introduced at the bottom skin, and nodes are selected to introduce the actuation loads, according to the TRIC principle. To model the morphing principle, the flexible skin is allowed to slide in the chord-wise and transverse direction to accommodate the required morphing shape under loads. Vertical deformations and rotations about the transverse and chord-wise axis are restrained. Figure 7 shows the boundary conditions employed in the FEM model.

These boundary conditions are chosen such as to allow the following morphing states, which are referred to as morphing subcases in the FSI model: (a) Bend Up, (b) Bend Down, (c) Twist.

The default structural solver used for the FSI analysis is the static linear solver SOL101 [41]. Additionally, SOL106 is implemented to run static non-linear analysis and to compare linear and non-linear structural model behaviour, which is presented in detail in section 5.2.

3.1.2. Actuation mechanism. A kinematic model of the actuation mechanism and the morphing interface has been constructed to facilitate the actuator sizing and the mechanical behaviour. The model presented in figure 7 shows (in a cross-sectional view) the FBD of the actuator force and moment equilibrium for the Bend Up case. The input to the actuator is the commanded angle, which in turn results in specific actuation torque (required to reach the desired position). Two essential aspects can be noted regarding the actuator input force to the morphing interface when examining the diagram: (a) the maximum actuator force, $F^{\max}$, that can be delivered at the attachment on the servo arm will increase by shortening the servo arm r_a, (b) the instantaneous actuator torque T_a required to balance or overcome the reaction forces at the morphing interface, F_r, is not linear for the range of travel of the actuator. The latter aspect results from the kinematic relationship of F_a, representing the actuator torque for a given actuator arm r_a and the linkage force F_l. Since F_a is a projection of the F_l normal to the servo arm ($F_\mathrm{a} < F_\mathrm{l}$), F_a and thus the amount of torque required by the actuator to balance or overcome the reaction forces are dependent to the relative position of the linkage system concerning the servo arm.

The relation of linkage force to δ_a is presented in the side view in figure 7, and is defined by the following relation:

$$F_\mathrm{l} = \frac{F_\mathrm{a}}{\cos(\delta_\mathrm{l})} \approx \frac{F_\mathrm{a}}{\cos(\delta_\mathrm{a})} \tag{1}$$

As the linkage length will be much greater than arm's length, δ_l can be approximated by δ_a.

Following the expression above, the actuator torque can be calculated as:

$$T_\mathrm{a} = F_\mathrm{l}\cos(\delta_\mathrm{l})\, r_\mathrm{a} \tag{2}$$

In this expression, the r_a represents the length of the torque arm, and the non-linear relationship between the actuator torque, T_a and the rotation angle, δ_l is reflected here by the cosine term. The following step was to establish an optimal torque arm such that the actuation loads are kept minimal within the desired morphing shapes, which is explained in section 5.3.2. The shapes are governed by the horizontal deflection range of the actuator (along F_l), indicated as x_a in figure 7.

3.2. Aerodynamic model

Aerodynamic behaviour is modelled using a 2D airfoil analysis based on strip theory. At each FSI loop iteration, the deformed wing shape is sliced at discretised span-wise sections to extract 2D deformed airfoils. The shape of the deformed airfoil is the input to XFOIL, which calculates the pressure distribution over the deformed airfoil [40]. This data is then used to calculate and interpolate the PLOADs corresponding to the structural mesh through the slicing of the airfoil. In NASTRAN, aerodynamic force is applied as static PLOAD, defined as a uniform PLOAD on the quadrilateral surface

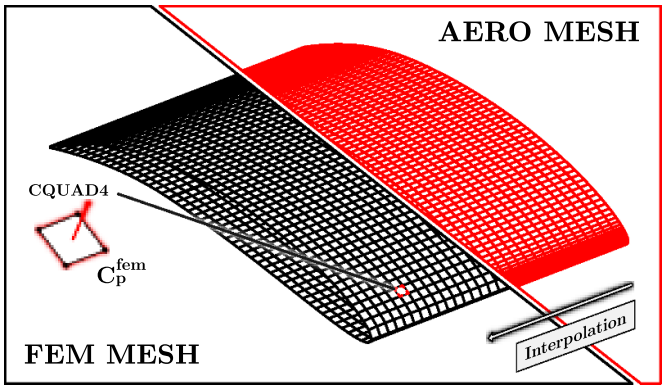

Figure 8. Mesh comparison FEM (left) and aero (right).

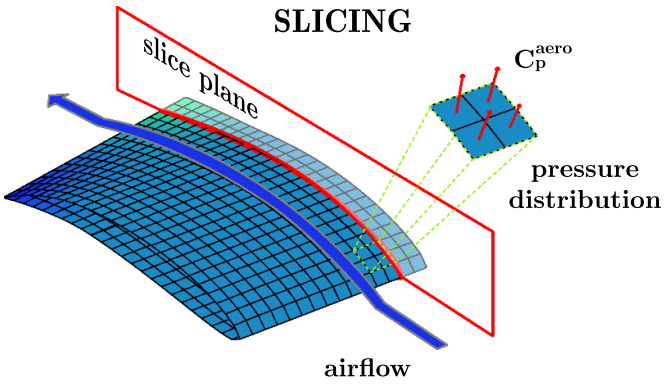

Figure 9. Airfoil slicing process.

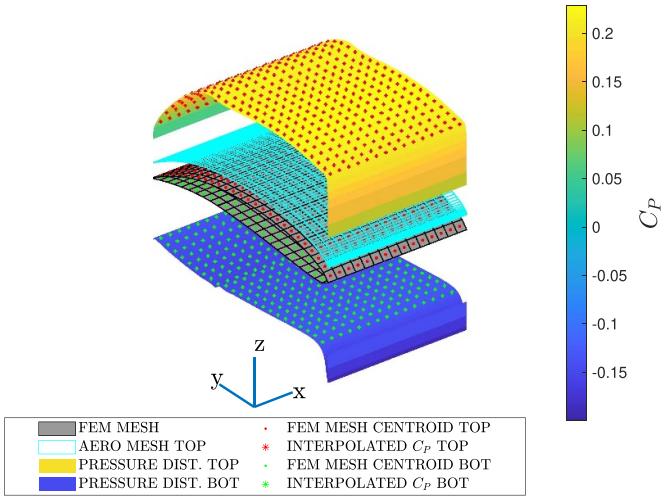

Figure 10. Coupling mechanism of aerodynamic loads to the FEM model shown for Bend down shape. Reproduced with permission from [31].

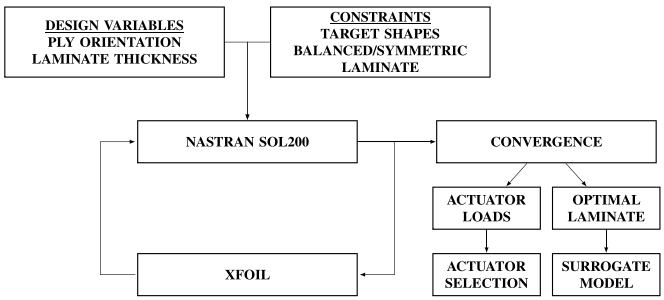

Figure 11. FSI optimisation framework. Reproduced with permission from [31].

(CQUAD4) comprised of four nodal positions, indicated in the bottom part of figure 8. Slice planes coincide with NASTRAN grid points to limit interpolation routines. This process of airfoil extraction is shown on the right of figure 9. The aerodynamic mesh is denser than the FEM mesh to improve the resolution of the pressure distribution, particularly in the LE and TE area. An additional interpolation routine is deployed to deal with the differences in meshes and sample the PLOADs on the corresponding quadrilateral surfaces of the structural mesh. This process is explained in the next section; the difference in the structural and aerodynamic mesh is presented in figure 8.

3.2.1. System coupling. As the meshes vary between the two models (i.e. the aerodynamic model has a higher resolution), an interpolation routine was used to transfer the pressure coefficient of aerodynamic mesh c_p^{aero}, to their appropriate centroid location in the FEM mesh c_p^{fem} values (figure 8). The interpolation function implements a gridded linear interpolation method based on Delaunay triangulation of the 2D grid data [42]. Since the interpolation is performed in 2D, the airfoil's upper and lower pressure distributions are sampled from the aerodynamic mesh separately and projected independently onto the x, y projection of the FEM mesh, acting as xy data sampling points for the interpolation. These sampling locations are the centroid of the mesh elements, as is illustrated in figure 10 [31]. Here again, the Bend Down case is considered as the target shape. The interpolation method uses MATLAB's griddata function. The interpolated pressure coefficients are then converted to PLOADs by evaluating the area of the corresponding mesh element. This is achieved using the NASTRAN PLOAD card [41], which allows evaluating static PLOAD directly from pressure coefficients. Appropriate scaling must be applied with the airspeed for the aerodynamic analysis. The conversion from non-dimensional pressure coefficient, cp to PLOAD pressure is performed as follows:

$$P_{LOAD} = -c_p^{fem} \frac{1}{2} \rho V_\infty^2 \tag{3}$$

The result of the interpolation routine can be visualised in figure 10.

3.3. Design optimisation

An optimised laminate design was desired, capable of attaining the three target morphing conditions utilising a minimum actuation load. For this purpose, an optimisation framework was constructed, which is presented in figure 11 [31].

3.3.1. Optimisation parameters. The core of the optimisation framework consists of NASTRAN's SOL200 optimiser

Table 1. Overview of input parameters, design variables and constraints of the optimization.

	Variable	Range	Unit
Input parameters	Angle of attack	$[-12, 0, 5]$	(°)
	V_∞	35	(m s^{-1})
Design variables	Ply angle	$[-90, -45, 45, 90]$	(°)
	Tickness	[1.65, 0.15]	(mm)
Objectives	Deformations	$[30, -20, \pm 20]$[a]	(mm)
	Target shapes	[Bend Up/Down, Twist]	(—)
Constraints	Laminate properties	Balanced/Symmetric	(—)
	Curvature constrain	[Bend Up/Down, Twist]	(—)

[a] traling edge deflection

[41], implementing the same FSI analysis strategy as shown in figure 5. For conciseness, the additional input blocks to the FSI loop are left out; the aerodynamic interaction is facilitated by XFOIL using the same convergence criteria. The three morphing conditions were considered subcases in the optimisation routine and were simultaneously optimised.

Input parameters, design variables and constraints used in the optimisation are presented in table 1. The input parameters of the optimisation framework are airspeed, V_∞ fixed at 35 m s^{-1} and the angles of attack corresponding to the most adverse aerodynamic loads within the stall limits of the airfoil. For the Bend Down case, $-12°$ of AoA was used, while for the Bend Up case, 5°. Ply orientation, and the thickness of the laminates were considered as the design variables for the laminate design.

3.3.2. Objectives. The optimisation objectives are represented by the tip deflection of 30, 20 and ±20 mm of Bend Up, Bend Down, and Twist subcases, respectively. A target of 30 mm was set for the Bend Up case due to the need for a larger negative lift increment of the asymmetric NACA 6510 airfoil. An overview of lift coefficients for various subcases is presented in table 4.

The optimisation outputs were the actuator loads needed for sizing the morphing mechanism and laminate design defined by ply orientation, layers and thicknesses.

3.3.3. Constraints. The optimisation was subject to design constraints in terms of laminate properties and curvature for the three subcases to ensure smooth morphing shapes.

Target shapes, defined by TE deflection, were subject to curvature constraint to avoid excessive local bending of the skin resulting in an aerodynamic penalty. The effect of the curvature constraints are shown in figures 12 and 13, respectively. The curvature constraints were enforced by prescribing predefined tolerances of every third node as shown in figure 13 for the Bend Up subcase. A similar approach was used also for the Bend Down and Twist subcase.

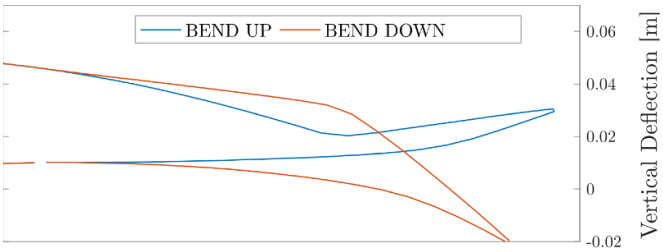

Figure 12. Deformed wing for Bend Up/Down case without curvature constraints.

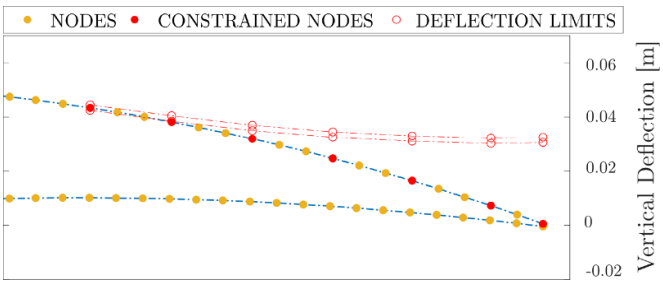

Figure 13. Deformed wing with enforced target shape on wing surface for the Bend Up subcase.

3.3.4. Optimisation model. Several optimisation strategies were investigated, which varied either the ply angle, the laminate thickness, or both.

Optimising both the ply orientation and the thickness across discretised strips of the morphing surface proved to be the least successful strategy for two reasons. Firstly, the high number of variables made it reasonably difficult to converge to a solution. Secondly, the ply continuity across the strips could not be ensured without additional constraints, which produced an unrealistic design for hand layup. When only the ply orientation was varied against a constant thickness, the resulting curvature of the morphed shapes exhibited kinks along the cord. The simplest approach, where the ply thickness gradually dropped and the thickness gradually varied, allowed sufficient flexibility in the chord-wise direction to eliminate the kinks. The finalized design is discussed in section 5.3.1.

3.4. Elastomeric skin design

A flexible connecting skin segment was investigated to prevent gaps between the morphing modules and ensure independent actuation between adjacent modules. The requirements for the connecting segments were to (a) ensure continuous morphing while not exceeding the continuous load requirements of the selected actuators, (b) the ability to sustain PLOADs for the operational flow regimes (up to 50 m s^{-1}), (c) allow post-manufacturing integration and (d) repair. Silicone material was selected for the skin as a connecting body due to ease of use, and a good compromise between strength and durability [43].

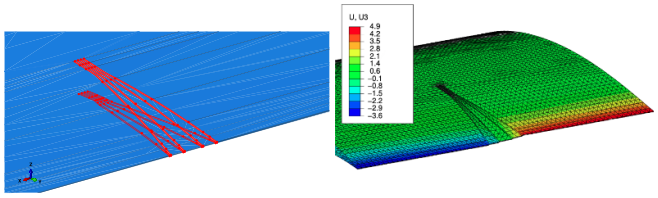

(a) Narrow slits filled with silicone.

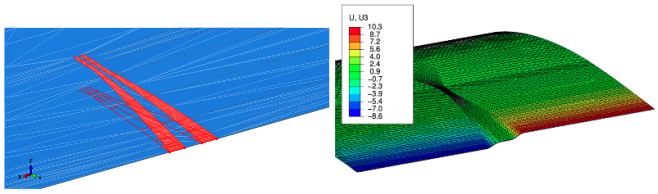

(b) Wide silicone patch reduced slit density.

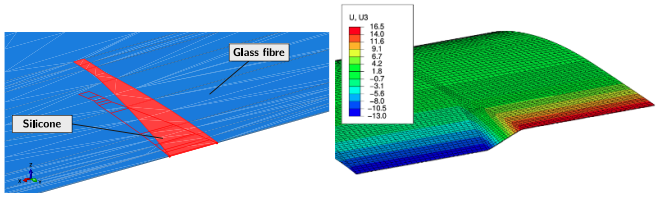

(c) Gap fully covered by silicone.

Figure 14. Elastomer skin design concepts.

FE models were built in Abaqus to study the elastomer material's flexibility and impact on the actuation loads. Various skin patch designs were considered with silicone-filled slits of varying width and slit density, as shown in figure 14. Through assessment of the morphing configurations, it was established that the critical aspect in elastomer integration was the amount of skin shearing required for asymmetric actuation between adjacent modules. The analysis with the FEM model revealed that the best compromise was a complete gap filled with an elastomer material. Further assessment was done using sample testing, as explained in section 4.2.

4. Design integration and testing

The wing design discussed in section 3 was used to build the wing demonstrator. A manufacturing procedure was established to allow the simultaneous integration of sensors and the optimised design implementation. The steps of this process are summarised in figure 15.

4.1. Manufacturing approach

The wing design comprised four parts (a) top skin, (b) bottom skin, (c) wing box and spars, (d) morphing TE. The wing skin was manufactured by vacuum-curing wet-laid glass fibre inside top and bottom polyurethane moulds. This manufacturing and assembly process is shown in sub-figures (A)–(D) of figure 15. The top skin was made in one pass, with the ply dropping incorporated at the TE (figure 15(A)). Due to the cut incorporated for the TRIC sliding edge, the bottom skin was made in two curing steps, the wing box skin and the morphing TE. Figures 15(B), (C) and 16 show the joining process and the assembly of various components in two wing halves. Figure 15(D) shows the final integration process. The skin seam along the trailing and LE were additionally reinforced with a fibre-glass wrapped foam wedge.

4.2. Elastomeric skin assessment

During the assessment of various silicone skin configurations, it was established that high-density slits, as shown in figure 14(a), did accommodate sufficient skin shearing to allow opposite actuation of adjacent modules within desired limits. It was observed that gradually increasing the gap between the adjacent modules and decreasing the slit density allowed more skin shearing, as suggested in section 3.4. Further, prototyping and testing using a 3D-printed jig validated the final elastomer design with a fully silicone-filled gap leading to the best results (figure 14(c)). The prototyping jig shown in figure 17 was actuated with two Volz DA-22-12-4112 servos and represented the connection between the adjacent modules. The jig was used to test the maximum deflection in Bend Up/Down and Twist morphing of various silicone skin samples from the Wacker Elastosil series. The moisture curing rubber silicone Wacker E41 [44] provided the best compromise between flexibility and bonding durability.

Once the silicone material and configuration were finalised from the jig, a manufacturing procedure was established to reproduce the design. A combination of 3D printed PLA (Polylactic Acid), and Teflon tape was used as a mould and release agent, respectively, defining the curvature between the module gaps. In the left and right of figure 15(D), the application process of the silicone is shown with the modules facing downward and the silicone applied from inside.

After curing the silicone and the final assessment of the elastomeric skin on the wing demonstrator, it was established that the joint was stiffer in shear than anticipated from the numerical analysis explained in section 3.4. A feasible limit for the actuation was found to be between $\pm 25°$. The manufactured demonstrator was subject to morphing characterisation tests explained, and further discussion is made in section 5.4.

4.3. DIC setup

A DIC static measurement was conducted on the top and bottom surfaces of the morphing modules, to validate the design and assess the capability of the wing demonstrator to attain the static target morphing shapes without aerodynamic load present.

4.3.1. Measurement procedure. The DIC test setup is shown in figure 18. The measurement system consisted of a Vic-3D stereo Q400 system and two cameras equipped with 15 mm focal length lenses [45]. The wing was placed upright. The top and the bottom skin of two morphing modules (modules 1 and 2) were covered in a speckle pattern. To capture the out-of-plane deformations, the two cameras were placed frontally, facing the patterned surfaces. Due to the lack of

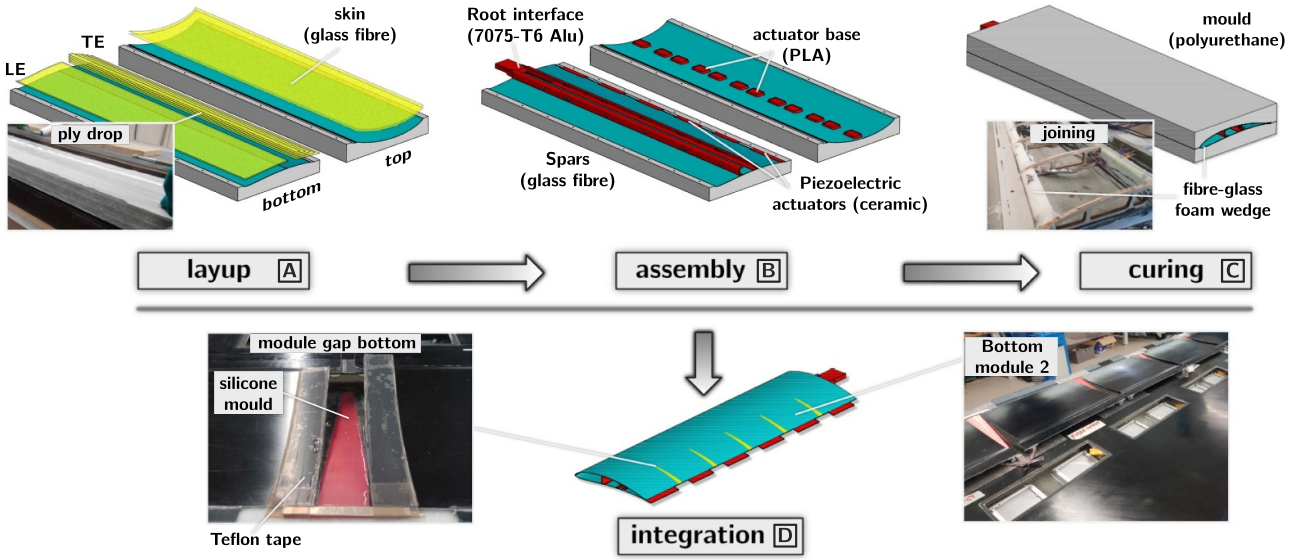

Figure 15. Wing manufacturing and integration process.

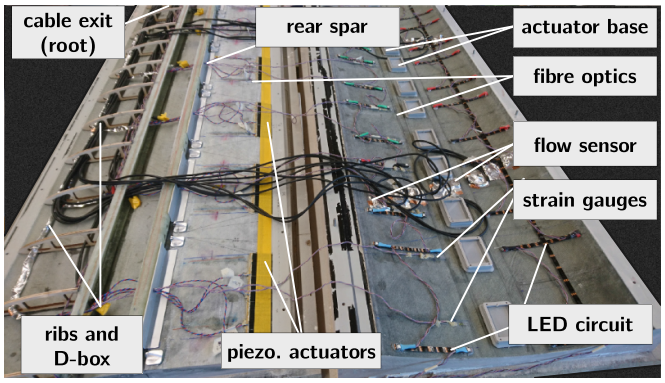

Figure 16. Assembly and integration of smart sensors, actuators and components in the wing.

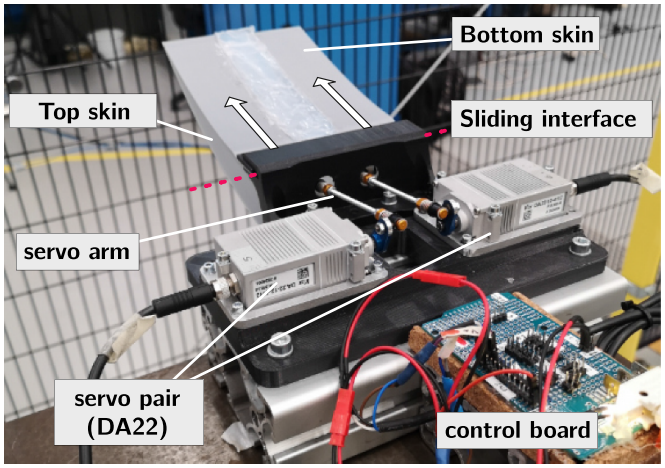

Figure 17. Testing jig components.

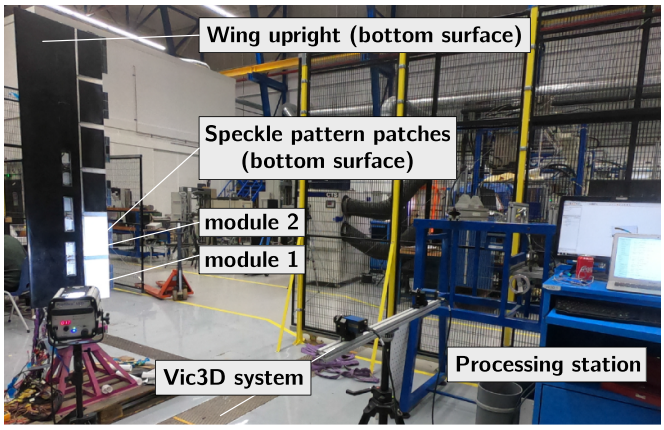

Figure 18. Vic3D DIC measurements system with two cameras. Reproduced with permission from [31].

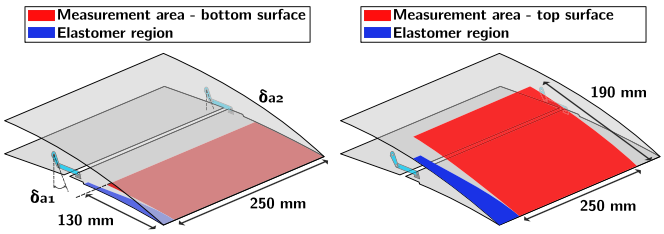

Figure 19. Top and bottom DIC measurement area. Reproduced with permission from [31].

visible overlap between the top and bottom skin needed for reconstruction, the measurements were obtained separately for the top and bottom surfaces with identical incremental actuation steps. The top and bottom surface measurements of the corresponding actuation steps were later merged manually during the post-processing to align the top and bottom surfaces.

The areas where the deformations were measured are indicated by the red patches in figure 19. The trailing 130 mm portion and 190 mm portion of the wing's lower and upper surface were analysed. The measurement area spanned 200 mm on the

Table 2. DIC measurement test matrix.

Condition	Trial 1		Trial 2		Shape
	δ_{a1} (°)	δ_{a2} (°)	δ_{a1} (°)	δ_{a2} (°)	
S.Bend Down (−)	−25	−25	−25	−25	
S.Bend Up (+)	+25	+25	+25	+25	
A.Bend Down (+/−)	−25	−25	+25	+25	
A.Bend Up (+/−)	+25	+25	−25	−25	

top and 250 mm on the bottom surface in the span-wise direction, centred on the module.

A measurement test matrix was designed to reflect the morphing design limits of the airfoil (shown in table 2). Both modules' maximum allowable actuation limits were chosen between positive 25° and negative 25°. The latter corresponded to the lower bound of approximately −4.5 mm chord-wise travel (Bend Down) within the guided slot, as established from the FEM model. The upper bound (Bend Up) was also limited to 4.5 mm (25°) after evaluating the allowable stretch in the resulting silicone skin for continuous operation.

The actuators were commanded in steps of 5° according to the scheme in table 2. In this table, a single actuator's Bend Up and Bend Down deflection corresponds to +25 and −25° actuation inputs, respectively. In total, four cases were considered, (a) Bend Down, (b) Bend Up, (c) Differential Bend Down and Differential Bend Up (d). In the symmetric arrangement, both modules moved in the same direction (both up or down), and in the asymmetric case, the modules moved opposite to each other (one up and one down). The latter cases were designed to assess the impact of the elastomer skin on the morphed shape, as due to the differential actuation, stretching and shearing was expected to take place in the elastomer. The DIC static measurements were repeated twice for the symmetric case (trial 1 and trial 2) and compared with the prediction generated by the numerical model developed earlier.

The numerical model did not include the elastomer skin. Hence it is expected that the numerical results show the best possible morphing case, where the elastomeric skin does not affect the morphing displacement of the module. The measurements for the asymmetric case were conducted similarly in two trials and compared to the symmetric cases.

4.3.1.1. Calibration procedure. The DIC measurements were transformed into the same reference frame used in the numerical model to perform comparative analyses. This was achieved by orienting the TE of the measured surfaces in line with the span-wise axis of the numerical model. A rotation about this axis was then performed to ensure that the undeformed surfaces aligned with the undeformed analysis model. The DIC stereo camera setup was calibrated with a standard calibration target of a 30 mm circular grid pattern. Verification of the DIC calibration was conducted on the top surface by comparing the TE tip deflections measured with DIC against deflections measured with a Vernier height gauge.

Furthermore, repeatability assessment was performed of the commanded morphed shape and the baseline shape in rest. The commanded actuator input configuration generated a repeatable morphed shape in both tests. Similarly, assessment of the baseline shape was performed to ensure commanded shapes arrived at the same baseline in the unloaded case (at rest). This assessment was found to correspond well to the expected NACA 6510 airfoil.

5. Results and discussion

The results and discussion are organised into three sections. First, the verification of the FSI tool and evaluation of non-linear structural effects are presented in sections 5.1 and 5.2. Then the outcome of the design optimisation is discussed in section 5.3. Finally, the validation of the morphing design is presented in section 5.4. In this last section, DIC measurement was conducted on the top and bottom surfaces of the morphing wing to assess the capability of attaining static target shapes.

In sections 5.1–5.3 aerodynamic load was applied as a pressure distribution generated by XFOIL to perform the structural design optimisation and asses the convergence of the framework. The comparison of the simulated and measured shapes on the manufactured wing in section 5.4 was performed without aerodynamic load.

5.1. FSI framework verification

A key aspect in the FSI framework and, in particular, the system coupling between the FEM and aerodynamics was to determine: (a) the required resolution of both meshes to eliminate discretisation effects due to the selected mesh density and (b) convergence criteria for the model to exit the FSI loop. Furthermore, an assessment was necessary of non-linear structural effects during large deformations. This was done by comparing linear and non-linear solutions in the FSI loop in section 5.2. The assessment was performed with aerodynamic loads applied on the structure.

5.1.1. Model convergence. The variation in deformations was analysed at each iteration as was indicated previously in figure 6, section 3.1, to evaluate the convergence of the FSI loop. The change in the magnitude of deformation is calculated at each node, where the sum of these differences represents the total deformation variance of the system at each iteration.

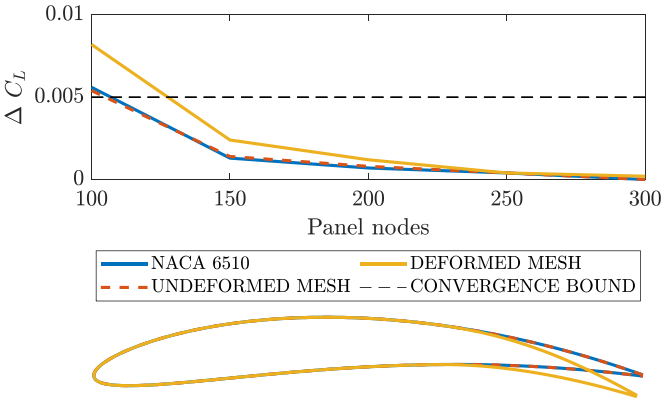

Figure 20. Aerodynamic mesh convergence study of the lift coefficient. Reproduced with permission from [31].

Multiple analyses were run to a high iteration count with 2D XFOIL analysis to obtain a satisfactory convergence bound. The change in lift coefficient and actuator input loads was monitored between each iteration in addition to the deformation variance. It was found that when the total deformation variance of the system was below 0.01, the variation in the lift coefficient was less than 0.0001, which represents 0.012% of the total C_L of baseline NACA6510. The actuation loads showed a variance of approximately 0.25% of peak load (approximately 0.15 N for all subcases)

With these negligible variations in lift and loads, the convergence performance was considered sufficient for the accuracy of this analysis, and the convergence bound was set with a deformation variance of 10^{-5}. Setting this bound means that the simulation terminates once the deformation variance $\leqslant 10^{-5}$.

5.1.2. Mesh convergence. A mesh convergence study was conducted on both meshes to determine a suitable resolution for the aerodynamic and structural mesh,

The meshes were refined consecutively, starting from the aerodynamic mesh, followed by the structural mesh with the aerodynamic mesh fixed. For the aerodynamic mesh, three morphed states of the airfoil were analysed: (a) XFOIL's default NACA6510, (b) undeformed structural mesh slice, and (c) deformed structural mesh slice. Peak Bend Up (30 mm), Bend Down (20 mm), and Twist (±20 mm) were considered for the structural mesh study. The analysis was completed at zero angle-of-attack and velocity of 30 m s^{-1}.

Results of the mesh resolution studies are presented in figures 20 and 21. For both meshes, convergence was evaluated by tracking the ΔC_L value. The convergence of the actuator input load was also assessed for the structural mesh.

As observed from figure 20, the 2D aerodynamic mesh converged at 140 nodes in a chord-wise direction. Therefore the default node XFOIL count of 160 nodes was maintained for future analyses. With this setting, the structural mesh converged beyond having 1500 elements. As the run time was sufficiently short, the mesh resolution was increased to apply ply dropping adequately, with more design freedom and accuracy.

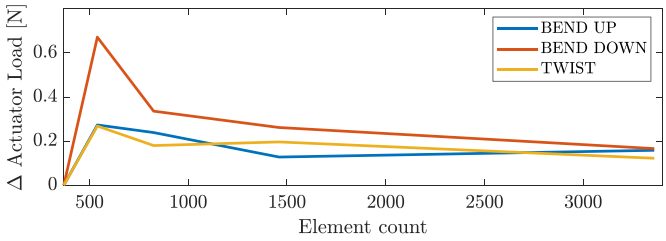

Figure 21. Structural mesh convergence study [31].

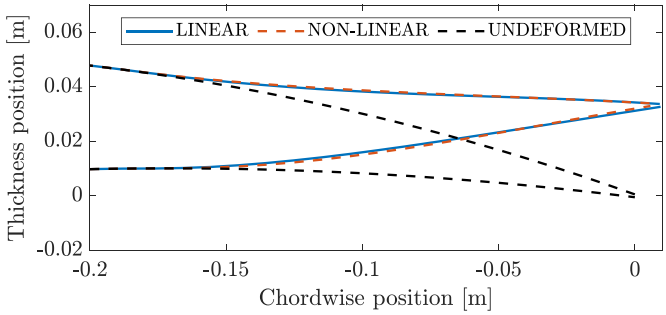

Figure 22. Comparison of linear and non-linear deformation for the case Bend Up [31]. (see if the act loads can be included).

This was achieved by increasing the mesh seed size to 10 mm, corresponding to 3360 elements.

5.2. Evaluation of non-linear solution

To study the impact of large deformations on the morphing surface and asses the validity of the linear FEM model, a comparison analysis was performed with a non-linear structural solver.

The comparison was performed by switching the linear static analysis (NASTRAN SOL101) to non-linear static analysis (NASTRAN SOL106). Since the analyses are performed statically, only the final deflected (converged) shape is considered, corresponding to the Bend Up, Bend Down and Twist cases.

Peak Bend Up/Down and Twist cases were evaluated at zero angles of attack and wind speed of 30 m s^{-1}. Mesh densities were kept in accordance with the outcomes of the mesh convergence study.

Comparison of lift coefficients is presented in table 3 [31]. Here in the last two columns, t_{lin} indicates the average execution times of linear solution in seconds, and $\Delta t_{\text{non-lin}}$, the average percentage increase of non-linear solution for each subcase. The benchmarking is performed over 10 FSI loops at 3° AoA and default meshing. A comparison of linear and non-linear deformations is presented in figure 22, indicated by a blue and red-dashed line, respectively. The difference in deformation is minimal, as can be seen by overlapping blue and red-dashed lines; however, differences of 3%–6% is observed for the in C_{L}, with the highest difference in Bend Up case.

Assessment of the actuation loads showed a 3% difference in the Bend Up case, with 140.7 N and 136.4 N for linear

Table 3. Comparison of linear and non-linear fem model for given design cases [31].

Subcase	$C_{L_{\text{lin}}}$ (—)	$C_{L_{\text{non-lin}}}$ (—)	ΔC_L (%)	t_{lin} (s)	$\Delta t_{\text{non-lin}}$ (%)
Bend Up	−0.277	−0.296	−6.589	31.2	370
Bend Down	1.464	1.423	2.801	36.5	271
Twist	0.823	0.847	−2.916	42.7	165
Unmorphed	0.825	0.825	—	—	—

and non-linear cases, respectively. In the Bend Down case, the loads were −80.4 N and −74.2 N, respectively, yielding an 8% difference. The loads are obtained for non-optimised, constant-thickness skin; hence lower loads are expected in the final optimised design, as discussed in more detail in section 5.3.2.

It must be noted, that the execution times for non-linear cases presented in table 3, are significantly higher. The percentage increase in time versus linear is between 165%–370%, which is undesirable for batch analysis. More importantly, the relatively small differences between linear and non-linear solutions will not significantly change the design regarding the required actuation load, as a margin is imposed for peak loads. This is discussed in the next section. Therefore, linear analysis is considered valid for design optimisation.

5.3. Design outcome

The optimisation routine described in section 3.3 was performed for the subcases Bend Up, Bend Down, and Twist (table 1) to generate the final laminate design for the morphing concept. Aerodynamic loads were applied in the analysis to ensure the skin was sized for the PLOADs, such that the deformations due to aerodynamic loads would be accounted for and the actuation forces were predicted correctly. Furthermore, the FSI framework described in the design methodology in section 3 was used to finalise the actuator selection.

5.3.1. Laminate design. During the optimisation process, the approach where the plies gradually dropped with the ply orientation fixed at ±45 allowed sufficient flexibility chord-wise to eliminate the kinks when morphing the control surfaces. Orienting the fibres along the span minimises the actuation force; however, this also compromises the chord-wise strength. The ±45 ply orientation provided the best compromise between the actuation force, bending stiffness and torsional stiffness. Furthermore, this configuration allowed symmetrically balanced ply drops and was easy to manufacture from readily available woven plies. Several composite materials were investigated, and fibre-glass designated US 7630 (MIL-Y-1140H) presented satisfactory results and was selected for use in the final design [46].

Figure 23 shows the undeformed morphing surface overlaid with the optimised thickness distribution. The colour map shows the number of plies required in each design region to build the morphing surface laminate.

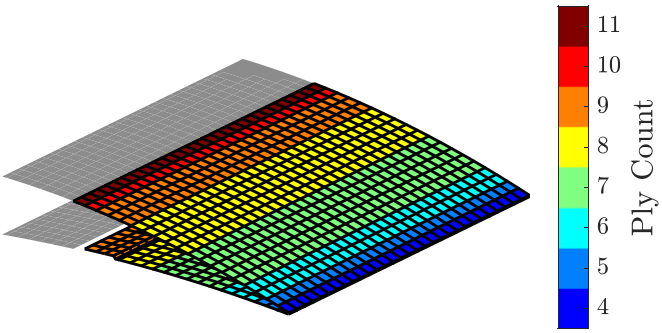

Figure 23. Ply dropping sequence.

The deformed morphing surfaces for the three subcases are presented in figure 24. They are superimposed on an undeformed surface to visualise the degree of deformations taking place. The colour map again represent the relative vertical deformations of the system.

5.3.2. Actuator loads. From the results of the optimisation routine, the peak actuation loads and the deflection range were determined. In table 4, the required input parameters for the three subcases are listed. Herein, the F_a and x_a indicate the actuation load and the horizontal deflection of actuator one, respectively.

The actuation load ranges from −60 N to +61 N. The deflection range of the actuator ranges from −4.5 to +6.5 mm. The resulting lift coefficients range from −1.7 to +2.2. This information aided in the selection of a suitable actuator for the application.

The deflection range, x_a, of the free edge of the morphing surface is shown in figure 25. With this information, the torque arm and rotation range, $\delta_{\text{act}}^{\max}$, of the servo could be set to calculate the torque requirements from the actuator. The actuator kinematic model was implemented according to the FBD illustrated in figure 7.

The design aimed to minimise the torque arm and increase the available actuation force F_{a}. This also resulted in an increased required range of rotation to cover the entire horizontal travel range. The range of rotation was limited to 40° to ensure that the linkage forces remained in the linear range.

The relation of linkage force to $\delta_a^{\max}$, defined by the equation (1), is presented in figure 26 [31]. Herein, it can be observed that the ratio of the linkage force relative to the actuator force rapidly moves further away from the 1:1 ratio beyond 40° of rotation. A higher linkage to actuator force ratio is

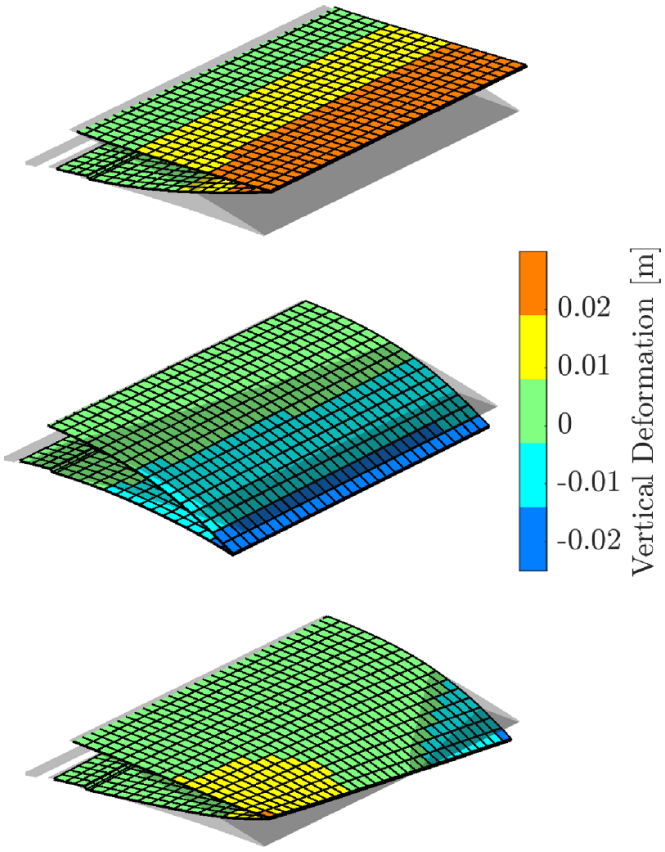

Figure 24. Deformed morphing surfaces for subcases, Bend Up (top), Bend Down (middle) and Twist (bottom). Reproduced with permission from [31].

Table 4. Actuator peak forces for various subcases. Reproduced with permission from [31].

Subcase	F_{a1} (N)	F_{a2} (N)	x_{a1} (mm)	x_{a2} (mm)	C_L (—)
Bend up	61	61	6.5	6.5	−1.7
Bend down	−60	−60	−4.5	−4.5	2.2
Twist	−50	23	4.5	−4.5	0.85

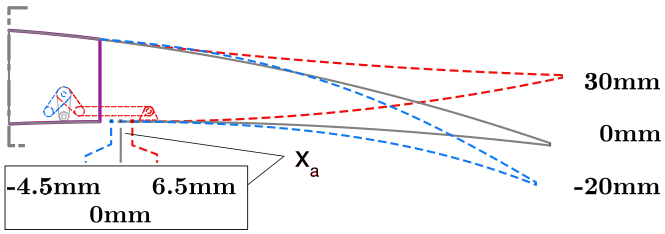

Figure 25. Horizontal travel range. Reproduced with permission from [31].

beneficial in actuation leverage. However, examining the FBD illustrated in figure 7 it can be deduced that the larger ratio comes at the price of reduced linear travel for higher rotation angles; therefore, ±40° was maintained as the maximum rotation range. For this range of rotation, the torque arm required for 7 mm of horizontal travel was 10 mm.

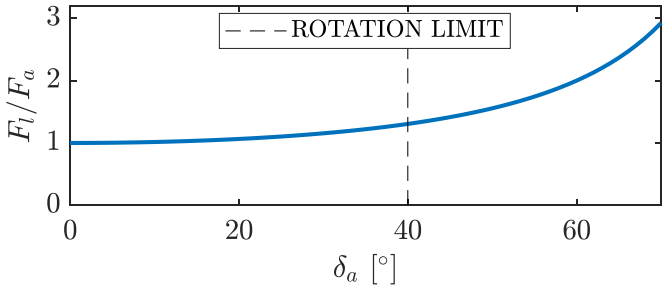

Figure 26. Linkage force as a function of servo rotation [31].

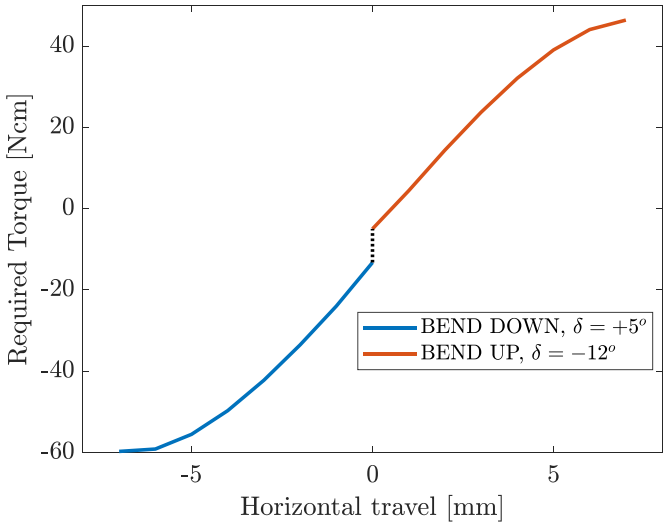

Figure 27. Torque versus horizontal travel, Bend Down and Bend Up considered [31].

The actuation loads were evaluated for the entire morphing range by incrementing horizontal travel at the actuation points, from −7 mm to 7 mm, in 1 mm increments to determine the actuator torque requirements. Only symmetric actuation was considered, as loads were most adverse in this scenario. The analysis was conducted at 30 m s^{-1}. To ensure most adverse aerodynamic loads were considered within the stall limits of the airfoil, the AOA was set to +5° for Bend Down cases and −12° for Bend Up cases. The data from these analyses are presented in figure 27. It can be seen that torque increases in a non-linear fashion, with peak torque requirements being nearly 45 Ncm for Bend Up and −60 Ncm for Bend Down. Note that, at zero travel, the lines do not coincide, as the analyses for the two cases were done at two different angles of attack.

For the peak loads presented in table 4, the peak torque required to actuate all morphing shapes at $V_\infty = 30$ m s^{-1} is ±60 Ncm. An operating margin of ≈35% of peak actuator torque was considered for continuous actuation at maximum free stream velocity and 1 Hz continuous sinusoidal actuation frequency at maximum rotation limits for the actuator selection. These requirements were selected to ensure the servo would not be used at 100% capacity during operation and would cope with the gust load alleviation task. These

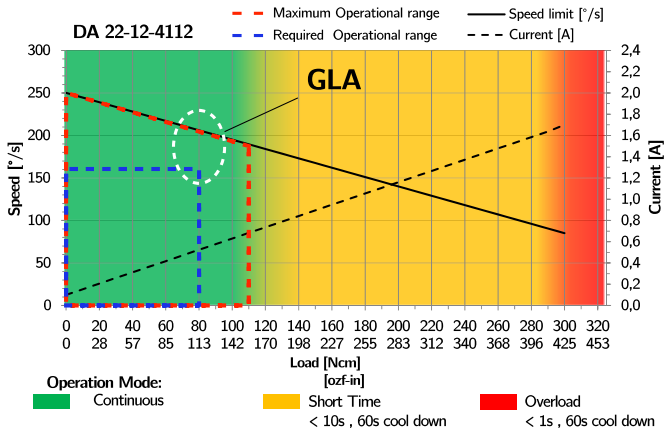

Figure 28. Volz da-22-12-4112 performance parameters in relation to control objectives [47].

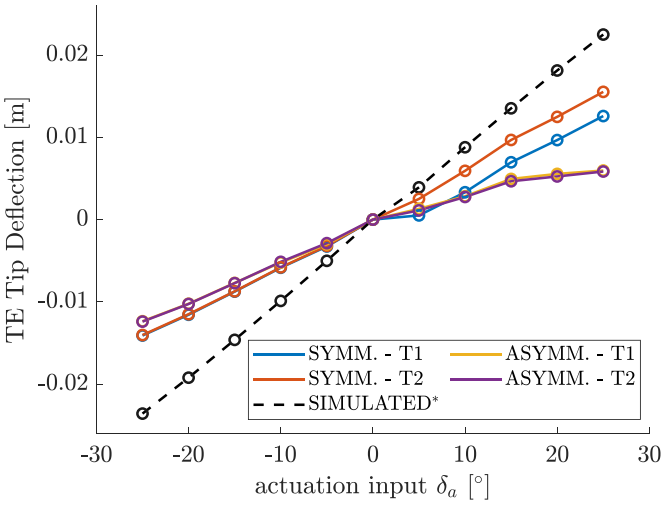

Figure 29. Comparison of tip deflection between numerical model and DIC measurement of symmetrical and asymmetrical cases $[25, -25]°$.

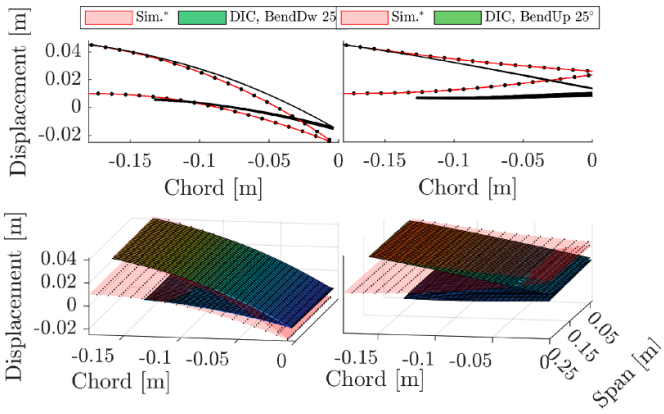

Figure 30. Comparison DIC and initial simulation prediction peak Bend Up and down symmetrical cases.

requirements resulted in ± 80 Ncm torque and 160 $^\circ$ s^{-1} continuous actuation at maximum load and maximum rotation limit ($\pm 40°$).

With these two requirements, the selection was made between the available actuator models of the servo manufacturer Volz [47]. This servo supplier was chosen due to the real-time actuator load and position feedback needed for the controller design. Volz DA 22-12-4112 was selected as it met both the continuous torque and bandwidth requirements within the available range of actuators. Figure 28 shows the performance specification data of the actuator published by the manufacturer [47]. The green region indicates the continuously operational range of the servo. As seen, the required peak torque requirement and the bandwidth indicated with a blue-dotted box fall within the servo's continuous operation range. At the peak torque of ± 80 Ncm, the actuator is capable of delivering a continuous speed of 210° s^{-1}, which corresponds to tracking of 1.3 Hz sinusoidal signal at 40° peak rotations. This is indicated by the maximum operational limit, the red-dotted box. The effectiveness of the gust load alleviation can be the highest near the region indicated by the dotted white line (maximum load and speed).

5.4. Morphing validation

A DIC static measurement was conducted on the top and bottom surfaces of the morphing modules to validate the design of static target morphing shapes. The validation of morphing shapes was performed without applied aerodynamic loads neither in the experiment nor in the numerical simulation.

The results between the DIC and the numerical model were compared by comparing the TE tip deflection and the airfoil shape. First, the symmetric cases shall be discussed in section 5.4.1, where both modules moved in the same direction. Then, the mechanical losses in the morphing system are discussed in section 5.4.2, and reflections are made on the simulation model. Finally, in section 5.4.3 the asymmetric cases are discussed, where the modules moved opposite to each other and the impact of the elastomer is significant.

5.4.1. Morphing assessment (symmetric). Figure 29 shows tip deflection for the entire actuation range for two trials in both symmetric (red, blue), asymmetric cases (purple, yellow) and estimation of the numerical model (black dotted).

Examining figure 29 for the symmetric case, the immediate observation yields that the linear curve predicted by the initial numerical model significantly overestimates the experimental tip deflection. This is observed more clearly in figure 30 which shows a comparison of measured and simulated peak tip deflections (top row) and 3D shape (bottom row).

The numerical model shows a linear slope between the actuator input range of $\pm 25°$. While this linear trend is upheld, in the 0° to $-25°$ range, the experimental curves have a much shallower slope than the prediction. On the opposite interval, the linear trend exhibits a dead-band for the actuator displacement between 0° and 5° in trials 1 and 2. The slope mismatch and the dead-band observations suggest that mechanical losses occur between the actuator input and the morphing shape, which the numerical model does not adequately capture. Consequently, this means that the morphed TE may fall

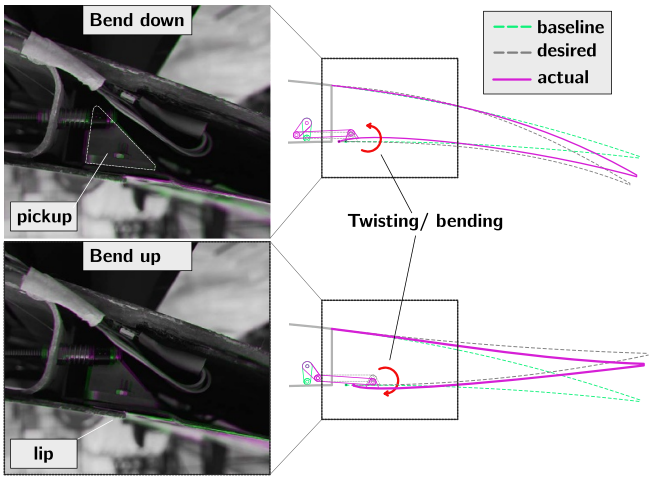

Figure 31. Backlash effect observed in Bend Up and Bend Down.

short of delivering the maximum expected lift increment when subject to a free stream velocity. A more in-depth analysis was set up to investigate the mechanical losses in the system during actuation, explained in the following sections.

5.4.2. Mechanical loss. After an initial evaluation of the numerical model, the mechanical system was observed more closely to investigate the potential source of mechanical losses during actuation. To this end, a visual inspection is performed during the Bend Up and Bend Down actuation strokes, and the image frames are processed with an image fusion algorithm shown in figure 31.

In this figure, composite difference images are created of the image sequences at the maximum strokes of the actuator (±25° actuator input), which correspond to Bend Up (bottom row) and Bend Down (top row) cases. The purple region indicates changes concerning the baseline position (zero ° actuator input). The image frame captures the cross-section view of the mechanism, where the linkage arm is attached to the skin interface via a triangular pickup component. The purple areas clearly show the twisting of pickup and bulging in/out occurring. The primary cause of this behaviour is attributed to the moment offset introduced as the servo arm pushes the vertex of the pickup and the relatively significant stiffness difference between the aluminium pickup body and the composite skin.

Observing the zoomed section of the bottom skin in figure 32 measured with the DIC, the findings from the visual inspection are confirmed. Here, the out-of-plane deformation of the bottom section of the skin near the lip is shown in peak Bend Up and Bend Down cases, in figures 32(A) and (B), respectively. Firstly, the lip bulges out during the bend upstroke and caves in during the Bend Down, reducing tip deflection. This behaviour is highlighted in the annotated cross-sectional view in figure 32 for both cases. The bulging out effect is observed clearly in figure 33, which shows the out-of-plane deflection in the 2D contour map for the Bend Up case in the top row of the figure. Secondly, from the 3D

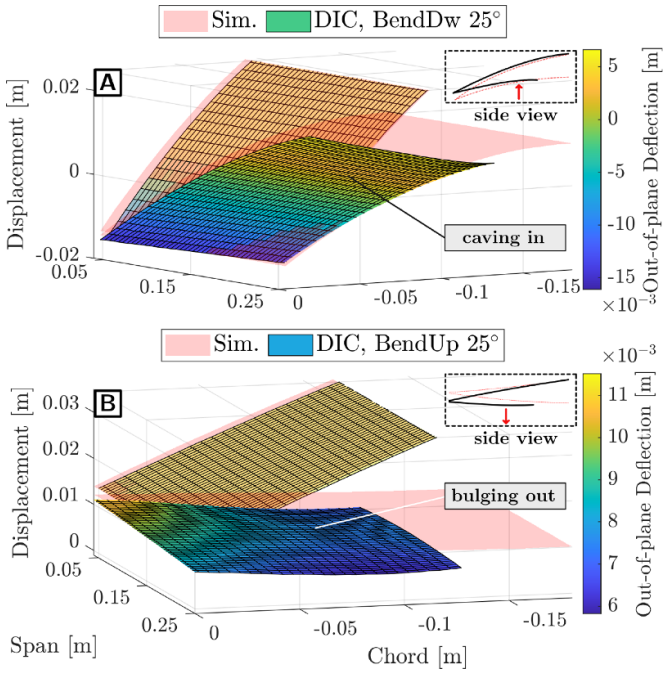

Figure 32. Bottom skin behaviour during peak Bend Up and Down with DIC in 3D view.

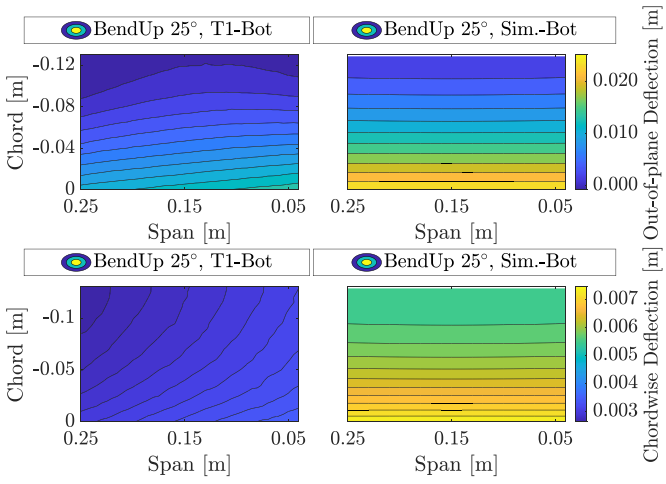

Figure 33. Comparison of symmetric Bend Up case for bottom surface.

view of the Bend Up case, it is observed that the bottom skin deforms unevenly along the span. This is revealed in better detail in the contour map of the chord-wise deflection shown in the bottom row of figure 33. As seen, the isolines are skewed towards the one end of the module, and the magnitude of chord-wise travel is nearly twice lower compared to the initial simulation.

5.4.2.1. Revised model. The undesired out-of-plane deformations observed in the measurements suggest that the actuator stroke is not fully converted to a chord-wise

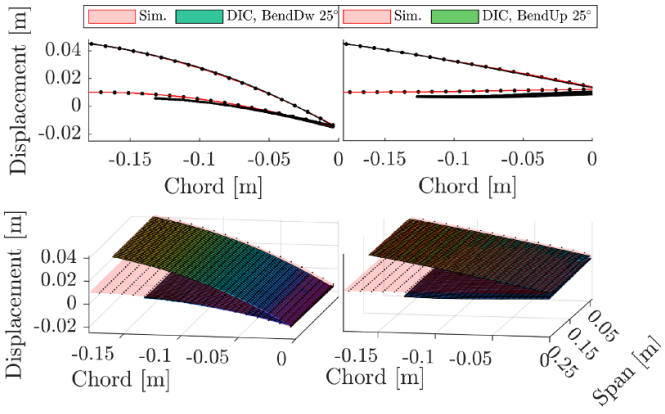

Figure 34. Comparison DIC and simulation peak Bend Up and Down symmetrical cases with corrected mapping.

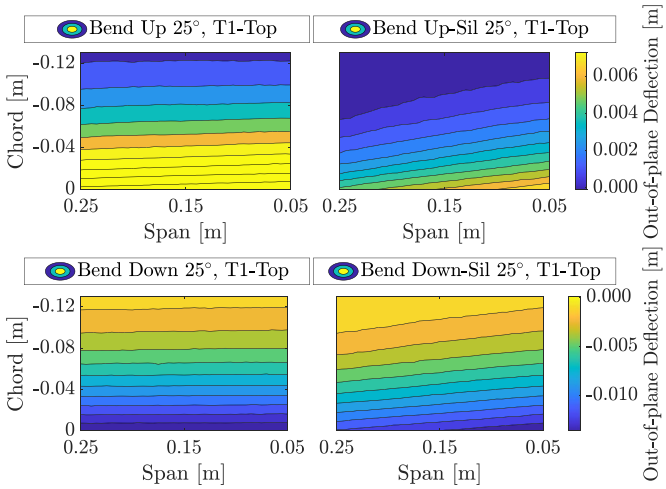

Figure 35. Comparison asymmetric cases top surface.

translation of the skin; instead, a significant part of the stroke is lost in twisting and bending of the bottom skin. From the perspective of the motion system, this behaviour can be characterised as backlash. This phenomenon is attributed to clearance inaccuracies and lost motion in mechanical systems, which can be partially compensated by increasing the actuator stroke. However, due to inaccuracies, the numerical model cannot adequately capture this complex behaviour and predict the tip deflection.

Adopting greater detail of actuation components and interfaces in the numerical model, e.g. accounting for guiding lip and the servo pickup, is a potential approach that can better estimate tip deflection. However, this will come at a high computational cost. Since the measured mapping follows a reasonably linear trend, shown in figure 29, a cost-efficient way to improve the prediction at peak input can be done by adjusting the linear mapping between the actuator input and tip deflection. Figure 34 shows the comparison between the revised model and the DIC measurements in symmetric, peak Bend Up and Down. The revised model yields a good agreement in deflection. However, the bulging out effect cannot be captured as shown in the airfoil shape in the top row. Consequently, this effect will be most apparent in the dead-band region, 0°–5°, where the linear trend does not hold, as shown in figure 30.

No aerodynamic load was applied in the experiment or in the numerical simulation to validate the morphing shapes. However, the design study, presented in sections 5.1–5.3, considered the aerodynamic load to ensure that the selected actuator could meet the required actuation load design targets. This approach, combined with the margin reserved for cord-wise translation, resulted in a conservative selection of the actuators, where a sufficient margin was ensured for (a) the actuation load and (b) the actuation stroke (servo rotation of up to 40 deg). Therefore, additional stiffness added due to manufacturing imperfections or the contribution of the elastomer can be accounted for by closing the control loop between the control surface deflection and actuator stroke. In the closed-loop control, the additional load and stroke budget can be used to meet the commanded tip deflection by observing the real-time tip deflection.

Robust, sensor-based control methods, such as the Incremental Nonlinear Dynamic Inversion, capable of mitigating model uncertainties through sensor feedback, are a suitable candidate [38]. In terms of sensors, embedded strain gauges, optical-fibres, or camera tracking can be used [48, 49].

5.4.3. Morphing assessment (asymmetric). The impact of the elastomer was assessed by evaluating the asymmetric cases measured by DIC, indicated by yellow and purple colours for trials 1 and 2, respectively, in figure 29. The modules were actuated in the opposite direction, generating tension and shearing in the elastomer skin. No comparison is made with the numerical model, as the main subject of interest was to observe the impact of the silicone skin on the experimental model. In trials 1 and 2, backlash is observed, but the trials show good agreement. The main difference between the symmetric cases is lower tip deflection. In particular, the peak tip deflection is significantly lower (≈0.065 m versus ≈0.012 for trial 1) for the interval 0°–25°, corresponding to module 1 bending upwards and module 2 downwards.

Observing the out-of-plane deflection in figure 35 for trial one on the top surface, Bend Down (bottom row) shows reasonable agreement; however, in the Bend Up case, the deformations are significantly reduced. The same measurement on the bottom surface, shown in figure 36, reveals a substantial bulging out effect; this is indicated with the highlighted annotation. This suggests that the actuation energy is consumed at peak deflection in bulging out of the skin rather than shearing the silicone skin. This also suggests that a better balance between the elastomer stiffness and the wing skin stiffness is needed to allow more shearing in the critical connecting areas.

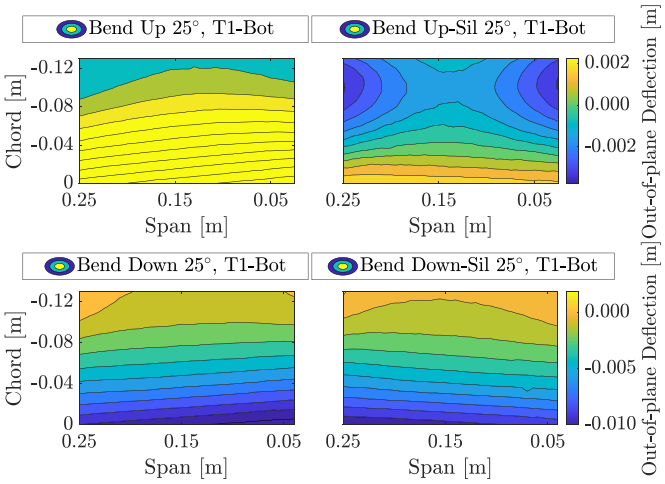

Figure 36. Comparison of peak asymmetric cases bottom surface.

6. Conclusion and outlook

A novel distributed morphing concept is presented, which addresses the drawbacks of the initial TRIC concept and allows variation of lift distribution locally along the span. The laminate design is optimised with an FSI optimisation framework taking into account the ply orientation, laminate thickness, laminate properties and actuation loads. Furthermore, a numerical and experimental study is performed to select a suitable elastomer design for inter-modular connection.

The desired morphing flexibility and manufacturability are met by a laminate design with fixed $\pm 45°$ ply orientation and gradual ply thickness dropping. The inter-modular connection is bridged with a wide silicon patch design, which impacts the actuation loads and flexibility the least. The manufacturability of the concept is demonstrated by the realisation of the modular wing demonstrator. The finalised concept is validated for the commanded target shapes with DIC measurements and visual characterisation.

A linear trend is observed during symmetric Bend Up and Down actuation, agreeing with the simulation. However, the validation study of the concept revealed a significant sensitivity to the backlash in the sliding interface and added stiffness due to the addition of the elastomer. Consequently, the peak deflections are lower than anticipated from the model. The measured input-output mappings are used to correct the model, improving peak deflection estimation. To improve the agreement with the manufactured morphing module, the structural stiffness of the numerical model should be updated with updated geometry, thicknesses and material properties. Furthermore, adding greater detail of the actuation components and interactions of the interfaces, such as the guiding lip and the servo pickup, can help to reflect the compliance of the real-life mechanism.

However, a significantly more complex model is required to capture the combined effect of backlash accurately and added stiffness of the elastomer, particularly at the lower input range. Capturing and integrating these effects in the design process, cost-efficiently, presents a challenge worth investigating in further studies.

While for the validation of the morphing shapes, no aerodynamic load was applied in the comparative analysis in both numerical and experimental results, the aerodynamic load was considered in the design study to ensure that the selected actuator could meet the required actuation load design targets. The approach resulted in conservative actuator selection, where a sufficient margin was accounted for in the actuation load and actuation stroke. Therefore, the additional actuation and stoke budget can be used to meet the commanded deflection with closed-loop control and account for stiffness added by manufacturing imperfections or the contribution of the elastomer.

In this regard, mitigating the backlash effect opens another opportunity for research that can be exploited with the current concept. A sensor-based compensator in the closed-loop controller, relying on accurate position measurements from the integrated sensors, is a possible approach. Finally, a further subject of ongoing research is investigating the impact of a more flexible wing structure on torsion and span-wise bending.

Data availability statement

The data that support the findings of this study are available upon reasonable request from the authors.

Acknowledgment

The authors would like to acknowledge Paul Lancelot for his assistance with implementing the NASTRAN SOL200 routine. The authors acknowledge Martin Weberschock at Weberschock Development in Gleichen, Germany, for his valuable contribution to the manufacturing process, wing construction and component assembly. Finally, the Delft University of Technology, Faculty of Aerospace Engineering, Department of Aerospace Structures and Materials is greatly acknowledged for the financial support to this work and the SmartX proje.

ORCID iDs

Tigran Mkhoyan https://orcid.org/0000-0001-8550-7393
Nisarg R Thakrar https://orcid.org/0000-0002-5358-1713
Roeland De Breuker https://orcid.org/0000-0002-7882-2173
Jurij Sodja https://orcid.org/0000-0001-8347-1438

References

[1] Lentink D, Müller U K, Stamhuis E J, De Kat R, Van Gestel W, Veldhuis L L, Henningsson P, Hedenström A, Videler J J and Van Leeuwen J L 2007 How swifts control their glide performance with morphing wings *Nature* **446** 1082–5

[2] Henningsson P, Hedenström A and Bomphrey R J 2014 Efficiency of lift production in flapping and gliding flight of swifts *PLoS One* **9** e90170

[3] Jex H R and Culick F E 1985 Flight control dynamics of the 1903 Wright Flyer *12th Atmospheric Flight Mechanics Conference AIAA Paper* (*Snowmass,CO*, *21 August 1985*) (Reston, VA: American Institute of Aeronautics and Astronautics) pp 534–48

[4] Weisshaar T A 2013 Morphing aircraft systems: historical perspectives and future challenges *J. Aircr.* **50** 337–53

[5] Barbarino S, Bilgen O, Ajaj R M, Friswell M I and Inman D J 2011 A review of morphing aircraft *J. Intell. Mater. Syst. Struct.* **22** 823–77

[6] Kintscher M, Geier S, Monner H P and Wiedemann M 2014 Investigation of multi-material laminates for smart droop nose devices *29th Congress of the Int. Council of the Aeronautical Sciences (ICAS 2014)* pp 1–11

[7] Sodja J, Martinez M J, Simpson J C and De Breuker R 2019 Experimental evaluation of a morphing leading edge concept *J. Intell. Mater. Syst. Struct.* **30** 2953–69

[8] Vasista S, De Gaspari A, Ricci S, Riemenschneider J, Monner H P and Van De Kamp B 2016 Compliant structures-based wing and wingtip morphing devices *Aircr. Eng. Aerosp. Technol.* **88** 311–30

[9] Previtali F, Arrieta A F and Ermanni P 2014 Performance of a three-dimensional morphing wing and comparison with a conventional wing *AIAA J.* **52** 2101–13

[10] Molinari G, Quack M, Arrieta A F, Morari M and Ermanni P 2015 Design, realization and structural testing of a compliant adaptable wing *Smart Mater. Struct.* **24** 105027

[11] Previtali F and Ermanni P 2012 Performance of a non-tapered 3D morphing wing with integrated compliant ribs *Smart Mater. Struct.* **21** 055008

[12] Molinari G, Arrieta A F and Ermanni P 2014 Aero-structural optimization of three-dimensional adaptive wings with embedded smart actuators *AIAA J.* **52** 1940–51

[13] Woods B K S, Dayyani I and Friswell M I 2015 Fluid/structure-interaction analysis of the fish-bone-active-camber morphing concept *J. Aircr.* **52** 307–19

[14] Woods B K, Bilgen O and Friswell M I 2014 Wind tunnel testing of the fish bone active camber morphing concept *J. Intell. Mater. Syst. Struct.* **25** 772–85

[15] Woods B K S, Friswell M I and Wereley N M 2014 Advanced kinematic tailoring for morphing aircraft actuation *AIAA J.* **52** 788–98

[16] Kota S, Hetrick J A, Osborn R, Paul D, Pendleton E, Flick P and Tilmann C 2003 Design and application of compliant mechanisms for morphing aircraft structures *Proc. SPIE* **5054** 24

[17] Kota S, Flick P and Collier F 2016 Flight testing of the FlexFloil^{TM} adaptive compliant trailing edge *54th AIAA Aerospace Sciences Meeting* (*San Diego, CA, USA*, *2 January 2016*) (https://doi.org/10.2514/6.2016-0036)

[18] Jenett B, Calisch S, Cellucci D, Cramer N, Gershenfeld N, Swei S and Cheung K C 2017 Digital morphing wing: active wing shaping concept using composite lattice-based cellular structures *Soft Robot.* **4** 33–48

[19] Cramer N B *et al* 2019 Elastic shape morphing of ultralight structures by programmable assembly *Smart Mater. Struct.* **28** 055006

[20] Keidel D, Fasel U and Ermanni P 2021 Concept investigation of a lightweight composite lattice morphing wing *AIAA J.* **59** 2242–50

[21] Bilgen O and Friswell M I 2014 Piezoceramic composite actuators for a solid-state variable-camber wing *J. Intell. Mater. Syst. Struct.* **25** 806–17

[22] Bilgen O, Butt L M, Day S R, Sossi C A, Weaver J P, Wolek A, Mason W H and Inman D J 2013 A novel unmanned aircraft with solid-state control surfaces: analysis and flight demonstration *J. Intell. Mater. Syst. Struct.* **24** 147–67

[23] Pankonien A M, Faria C T and Inman D J 2015 Synergistic smart morphing aileron: experimental quasi-static performance characterization *J. Intell. Mater. Syst. Struct.* **26** 1179–90

[24] Mistry M and Gandhi F 2015 Design, fabrication and benchtop testing of a helicopter rotor blade section with warp-induced spanwise camber variation *J. Intell. Mater. Syst. Struct.* **26** 1272–89

[25] Nguyen N, Lebofsky S, Ting E, Kaul U, Chaparro D and Urnes J 2015 Development of variable camber continuous trailing edge flap for performance adaptive aeroelastic wing *SAE AeroTech Congress & Exhibition* (*Seattle, WA, USA*, *September 22 2015*) (https://doi.org/10.4271/2015-01-2565)

[26] Ferrier Y L, Nguyen N T, Ting E, Chaparro D, Wang X, de Visser C C and Chu Q P 2018 Active gust load alleviation of high-aspect ratio flexible wing aircraft *2018 AIAA Guidance, Navigation, and Control Conference* (*Reston, VA*, *7 January 2018*) (American Institute of Aeronautics and Astronautics) (https://doi.org/10.2514/6.2018-0620)

[27] Nguyen N, Ting E, Chaparro D, Drew M and Swei S 2017 Multi-objective flight control for drag minimization and load alleviation of high-aspect ratio flexiblewing aircraft *58th AIAA/ASCE/AHS/ASC Structures, Structural Dynamics, and Materials Conference* (*Grapevine, TX, USA*, *5 January 2017*) p 1589

[28] Werter N P, Sodja J, Spirlet G and De Breuker R 2016 Design and experiments of a warp induced camber and twist morphing leading and trailing edge device *24th AIAA/AHS Adaptive Structures Conf.* (*San Diego, CA, USA*, *1 January 2016*) (https://doi.org/10.2514/6.2016-0315)

[29] Wang X, Mkhoyan T and de Breuker R 2022 Nonlinear incremental control for flexible aircraft trajectory tracking and load alleviation *J. Guid. Control Dyn.* **45** 1

[30] Project SmartX 2022 (available at: www.tudelft.nl/en/ae/smartx)

[31] Mkhoyan T, Thakrar N R, De Breuker R and Sodja J 2020 Design of a smart morphing wing using integrated and distributed trailing edge camber morphing *ASME 2020 Conf. on Smart Materials, Adaptive Structures and Intelligent Systems* (*Irwine, CA, USA*, *4 November 2020*) (American Society of Mechanical Engineers) (https://doi.org/10.1115/smasis2020-2370)

[32] Mkhoyan T 2022 Autonomous smart morphing wing: development, realisation & validation *PhD Thesis* Delft University of Technology (https://doi.org/10.4233/uuid:b1c97841-fda7-420c-8feb-f1145faa531c)

[33] De Breuker R, Mkhoyan T, Nazeer N, Stuber V L, Wang X, Mkhoyan A, Groves R M, van der Zwaag S and Sodja J 2022 Overview of the SmartX wing technology integrator *Actuators* **11** 10

[34] Vos R, Gürdal Z and Abdalla M 2010 Mechanism for warp-controlled twist of a morphing wing *J. Aircr.* **47** 450–7

[35] Drew M, Hashemi K E, Cramer N and Nguyen N T 2019 Multi-objective optimal control of the 6-DoF aeroservoelastic common research model with aspect ratio 13.5 wing *AIAA Scitech 2019 Forum,* (*San Diego, CA, USA*, *6 January 2019*) (https://doi.org/10.2514/6.2019-0220)

[36] Pereira M d F, Kolmanovsky I, Cesnik C E and Vetrano F 2019 Model predictive control architectures for maneuver load alleviation in very flexible aircraft *AIAA Scitech 2019 Forum* (*San Diego, CA, USA*, *6 Jan 2019*) pp 420–32

[37] Dillsaver M J, Cesnik C E and Kolmanovsky I V 2013 Trajectory control of very flexible aircraft with gust disturbance *AIAA Atmospheric Flight Mechanics (AFM) Conf. AIAA Atmospheric Flight Mechanics (AFM) Conf.* (*Boston, MA, USA*, *15 August 2013*) (American Institute of Aeronautics and Astronautics) (https://doi.org/10.2514/6.2013-4745)

[38] Wang X, Van Kampen E, Chu Q P and De Breuker R 2019 Flexible aircraft gust load alleviation with incremental nonlinear dynamic inversion *J. Guid. Control Dyn.* **42** 1519–36

[39] MacNeal R.H. and McCormick C.W. 1970 The NASTRAN computer program for structural analysis *Comput. Struct.* **1** 3

[40] Drela M 1989 *Xfoil: An Analysis and Design System for Low Reynolds Number Airfoils* vol 54 (Berlin: Springer)

[41] Siemens 2014 Design Sensitivity and Optimization User's Guide *Techncial Report* (Siemens Product Lifecycle Management Software) (available at: https://docs.plm.automation.siemens.com/data_services/resources/nxnastran/10/help/en_US/tdocExt/pdf/optimization.pdf)

[42] Watson D F 1992 *Contouring: A Guide to the Analysis and Display of Spatial Data* 1 (Oxford: Pergamon)

[43] Thill C, Etches J, Bond I, Potter K and Weaver P 2008 Morphing skins *Aeronaut. J.* **112** 117–39

[44] Wacker 2020 ELASTOSIL ® E41 TRANSPARENT *Techncial Report* (Wacker) (available at: www.wacker.com/h/en-us/medias/ELASTOSIL-E41-TRANSPARENT-en-2021.07.15.pdf)

[45] Correlated Solutions 2020 VIC-3D 9 with iris system specifications VIC-3D 9 system specifications *Techncial Report* (Correlated Solutions) (available at: www.correlatedsolutions.com/wp-content/uploads/2020/09/VIC-3D-9-System-Specs.pdf)

[46] Interglas 2010 lass filament fabrics for plastics reinforcement *Techncial Report* (Interglas) (available at: www.swiss-composite.ch/pdf/t-Glas-163g-92110-FK144-e.pdf)

[47] Volz 2013 Volz DA 22 technical specification *Techncial Report* (Volz Servos GmbH) (available at: https://volz-servos.com/resources/Downloads/Datasheets/DA-22_Datasheet_uni_revised.pdf)

[48] Mkhoyan T, de Visser C C and De Breuker R 2021 Adaptive real-time clustering method for dynamic visual tracking of very flexible wings *J. Aerosp. Inf. Syst.* **18** 58–79

[49] Mkhoyan T, de Visser C C and De Breuker R 2021 Adaptive state estimation and real-time tracking of aeroelastic wings with augmented kalman filter and kernelized correlation filter *AIAA Scitech 2021 Forum* (*Virtual*, *4 January 2021*) p 0666